UNIVERSITY OF THESSALY
SCHOOL OF ENGINEERING
DEPARTMENT OF MECHANICAL ENGINEERING

A STUDY ON THE EFFECTS OF WASTEGATE ANGLE ON AFTERTREATMENT HEAT UP DURING COLD START

by

AIKATERINI KARAMARIOGLOU

Submitted in partial fulfillment of the requirements for the degree of Diploma in Mechanical Engineering at the University of Thessaly

Volos, 2023

UNIVERSITY OF THESSALY
SCHOOL OF ENGINEERING
DEPARTMENT OF MECHANICAL ENGINEERING

A STUDY ON THE EFFECTS OF WASTEGATE ANGLE ON AFTERTREATMENT HEAT UP DURING COLD START

by

AIKATERINI KARAMARIOGLOU

Submitted in partial fulfillment of the requirements for the degree of Diploma in Mechanical Engineering at the University of Thessaly

Volos, 2023

Approved by the Committee on Final Examination:

Advisor	Dr. Konstantinos Ritos, Assistant Professor, Department of Mechanical Engineering, University of Thessaly
Member	Dr. Costas Papadimitriou, Professor, Department of Mechanical Engineering, University of Thessaly
Member	Dr. Tassos Stamatelos, Professor, Department of Mechanical Engineering, University of Thessaly

Date Approved: November 09, 2023

ACKNOWLEDGEMENTS

I would like to begin by expressing my deepest appreciation to my manager, Mr. Raduz Zahoransky and my colleagues at Garrett Motion Czech Republic for giving me the opportunity to work with them and providing me with valuable knowledge and support for the completion of my thesis as well as overall guidance through my first steps as an engineer.

I would especially like to thank my Professor Dr. Konstantinos Ritos, without whom I could not have undertaken this journey, for his constant support and mentoring during these past months. His knowledge and experience helped me immensely to complete this research. Special thanks to the committee, Dr Costas Papadimitriou and Dr Tassos Stamatelos for the tedious studying of my thesis and their valuable help and feedback.

I would be remiss in not mentioning Michal Planka, Martin Babak, Tomas Hebnar, Petr Malec and many more that trained me and helped me to overcome the challenges of my thesis by providing me with all the required software knowledge and guidance.

During my internship, I had the pleasure of working with amazing individuals who inspired me and gave me both professional and moral support. By believing in me and keeping my spirits high I was able to work through any difficulties being in a foreign country and working for the first time in the industry. Thank you Gaëtan, Théo, Sam and every single one of my friends and colleagues that impacted me since coming to Czech Republic. A special thanks to my former colleague and friend Thomas Zanon for motivating me constantly and staying with me during late office hours while I was waiting for my simulations to finish.

Lastly, I would like to thank my family, my friends and classmates from Greece and my professors, who were all there to see me grow as an engineer and as a person and shaped my beginnings. Most notably, I will always appreciate the support of my close friends Semina, Aimilia and Giannis, who are abroad like me trying to achieve their goals.

A STUDY ON THE EFFECTS OF WASTEGATE ANGLE ON AFTERTREATMENT HEAT UP DURING COLD START

AIKATERINI KARAMARIOGLOU

Department of Mechanical Engineering, University of Thessaly

Supervisor: Dr Konstantinos Ritos

Associate Professor of Turbomachinery

ABSTRACT

In today's world, governments and regulatory bodies are increasingly confronted with pressing environmental concerns, tightening the emission limits in response. As a result, the automotive industry faces a technological challenge, with a growing awareness of its impact on the climate crisis and the urgent need to mitigate vehicular emissions by implementing new strategies and innovations. This is particularly pertinent in the realm of heavy-duty diesel vehicles, which play a substantial role in commercial transportation and industrial activities, and need to comply with various standards that are region dependent.

Future emissions regulations [EPA27, EuroVII], focus on further reduction of nitrogen oxides [NOx], carbon dioxide emissions [CO_2] and other particulates with a specific focus on the cold start. Aftertreatment systems have been the center of attention with continuous improvements being made in order to increase their efficiency and to minimize the time required to reach optimal operating temperatures.

Turbochargers have become integral components of modern internal combustion engines, offering improved performance and efficiency. However, their potential as thermal energy sources for aftertreatment systems remains underutilized. This thesis investigates the feasibility and effectiveness of harnessing the turbine outlet flow from turbochargers to expedite the heating process of aftertreatment systems. Through a comprehensive study combining Computational Fluid Dynamics (CFD) and physical testing, a robust turbine model is produced and validated followed by a preliminary approach in modelling the aftertreatment system. The behavior of the turbocharger - catalyst system is examined in an attempt to monitor the effects of the by-pass valve's positioning to the catalyst light-off time. The results reveal the potential for substantial heat recovery from the exhaust gases, which can significantly reduce the warm-up time required for aftertreatment components.

Ultimately, the present Diploma thesis addresses a sustainable solution to enhance the aftertreatment's efficiency contributing to the automotive industry's attempts towards a cleaner, more environmentally responsible future.

Key words: turbochargers, after treatment, emission standards, automotive industry, climate change, turbine flow, turbocharger, SCR, porous media, wastegate, by-pass valve, Computational Fluid Dynamics, ANSYS CFX

ΜΕΛΕΤΗ ΤΗΣ ΕΠΙΔΡΑΣΗΣ ΤΗΣ ΓΩΝΙΑΣ ΒΑΛΒΙΔΑΣ ΠΑΡΑΚΑΜΨΗΣ ΣΤΗΝ ΑΠΟΔΟΣΗ ΣΥΣΤΗΜΑΤΟΣ ΜΕΤΕΠΕΞΕΡΓΑΣΙΑΣ ΚΑΥΣΑΕΡΙΩΝ ΚΑΤΑ ΤΗΝ ΨΥΧΡΗ ΕΚΚΙΝΗΣΗ

ΑΙΚΑΤΕΡΙΝΗ ΚΑΡΑΜΑΡΙΟΓΛΟΥ

Τμήμα Μηχανολόγων Μηχανικών, Πανεπιστήμιο Θεσσαλίας, 2023

Επιβλέπων Καθηγητής: Δρ. Κωνσταντίνος Ρήτος,

Καθηγητής Στροβιλομηχανών

ΠΕΡΙΛΗΨΗ

Την σήμερον ημέρα, οι κυβερνήσεις καθώς και οι αντίστοιχες ρυθμιστικές αρχές έρχονται ολοένα και περισσότερο αντιμέτωπες με αυξανόμενες περιβαλλοντικές ανησυχίες, οδηγώντας στην επιβολή αυστηρότερων ορίων εκπομπών. Ως αποτέλεσμα, η αυτοκινητοβιομηχανία, έχοντας επίγνωση του περιβαλλοντικού αντίκτυπου που επιφέρει, αντιμετωπίζει μια τεχνολογική πρόκληση με στόχο να μετριάσει τις εκπομπές των οχημάτων εφαρμόζοντας νέες στρατηγικές και καινοτομίες. Αυτό αφορά ιδιαίτερα τα ντίζελ οχήματα επαγγελματικής χρήσεως, τα οποία κατέχουν σημαντικό ρόλο στις εμπορικές μεταφορές και τις βιομηχανικές δραστηριότητες και πρέπει να συμβαδίζουν με τα διάφορα πρότυπα εκπομπών, διαφορετικά ανά περιοχή.

Τα μελλοντικά πρότυπα εκπομπών [EPA27, EuroVII] επικεντρώνονται στην περαιτέρω μείωση των οξειδίων του αζώτου [NOx], των εκπομπών διοξειδίου του άνθρακα [CO2] και άλλων σωματιδίων με ιδιαίτερη έμφαση στην εκκίνηση με ψυχρό κινητήρα. Κέντρο του ενδιαφέροντος αποτελούν τα συστήματα μετεπεξεργασίας ,καθώς γίνονται συνεχείς προσπάθειες για την αύξηση της αποδοτικότητάς τους και την ελαχιστοποίηση του χρόνου που απαιτείται ώστε να επιτευχθεί η βέλτιστη θερμοκρασία λειτουργίας .

Οι στροβιλοσυμπιεστές έχουν γίνει αναπόσπαστα εξαρτήματα των σύγχρονων κινητήρων εσωτερικής καύσης, προσφέροντας βελτιωμένη απόδοση και αποδοτικότητα. Ωστόσο, οι δυνατότητές τους ως πηγές θερμικής ενέργειας για τα συστήματα

μετεπεξεργασίας παραμένουν ανεκμετάλλευτες. Η παρούσα διατριβή διερευνά, πρωτίστως τη δυνατότητα , και εν συνεχεία την αποτελεσματικότητα της αξιοποίησης της ροής εξόδου των καυσαερίων από την τουρμπίνα, για την επιτάχυνση της διαδικασίας θέρμανσης του καταλύτη. Μέσω μιας ολοκληρωμένης μελέτης που συνδυάζει υπολογιστική ρευστοδυναμική (CFD) και φυσικές δοκιμές, παρατίθεται και αξιολογείται ένα αξιόπιστο μοντέλο τουρμπίνας, το οποίο συνοδεύεται από μια πρωταρχική προσέγγιση στη μοντελοποίηση του συστήματος μετεπεξεργασίας. Η συμπεριφορά του συστήματος στροβιλοσυμπιεστή - καταλύτη μελετάται σε μια προσπάθεια παρακολούθησης των επιδράσεων της γωνίας της βαλβίδας παράκαμψης στο χρόνο ανάφλεξης του καταλύτη. Τα αποτελέσματα που προκύπτουν, αποκαλύπτουν τη δυνατότητα σημαντικής ανάκτησης θερμότητας από τα καυσαέρια, η οποία μπορεί να μειώσει σημαντικά τον απαιτούμενο χρόνο προθέρμανσης.

Εν κατακλείδι, , η παρούσα διπλωματική εργασία πραγματεύεται μια βιώσιμη λύση για τη βελτίωση της απόδοσης του καταλύτη, συμβάλλοντας στις προσπάθειες της αυτοκινητοβιομηχανίας για ένα καθαρότερο, περιβαλλοντικά υπεύθυνο μέλλον.

Λέξεις κλειδιά: υπερσυμπιεστές, μετεπεξεργασία, πρότυπα εκπομπών καυσαερίων, αυτοκινητοβιομηχανία, κλιματική αλλαγή, ροή στροβιλοσυμπιεστή, καταλύτης, πορώδη μέσα, βαλβίδα παράκαμψης, Υπολογιστική Ρευστοδυναμική, ANSYS CFX

TABLE OF CONTENTS

LIST OF FIGURES

LIST OF TABLES

LIST OF ABBREVIATIONS

Abbreviation	**Definition**
3D	Three Dimensional
B.C	Boundary Condition
BSR	Blade Speed Ratio
CAD	Computer Aided Design
CBE1	Common Based Engine 1
CFD	Computational Fluid Dynamics
CHRA	Center Housing Rotating Assembly
CV	Commercial Vehicles
DNS	Direct Navier Stokes
DOC	Diesel Oxidation Catalyst

DOE	Design Of Experiment
DPF	Diesel Particulate Filter
ECU	Electronic Control Unit
EPA	Environmental Protection Agency
FT	Full Turbine
GGI	General Grid Interface
ICE	Internal Combustion Engine
ID	Inner Diameter
LES	Large Eddy Simulation
MPM	Mixing Plane Model
MRF	Moving Reference Frame
OD	Outer Diameter
PR	Pressure Ratio
RANS	Reynold-Averaged Navier Stokes
SBP	Single Blade Passage
SCR	Selective Catalytic Reactor
SST	Shear Stress Transport
SWA	Shaft – Wheel Assembly
THS	Turbine Housing
VNT	Variable Nozzle Turbine
WG	Wastegate
DP	Design Point

1. Introduction

Turbocharging technology has established itself as synonymous with enhanced engine capabilities and reduced emissions, thus solidifying turbochargers as pivotal components in internal combustion engines for many years. Their potential is yet to be fully explored, as new technological advancements are continuously being made striving for better performance. Except for the active ways a turbocharger can aid in the emission's reduction, there are passive ways to further profit form their operation, one of which will be explored in this thesis.

Extensive research has been conducted on the utilization of the by-pass flow for aftertreatment heat-up in passenger vehicles, with research contributions from both Garrett's database and independent studies. However, when it comes to commercial vehicles applications, this concept represents a relatively new frontier, involving distinct challenges and parameters. These challenges span from the intricacies of the turbocharger simulation itself, to the integration of the Selective Catalytic Reactor (SCR).

The scope of the thesis is the modelling and simulation of a [redacted], twin-scroll turbocharger with an internal wastegate, and the in-depth analysis of the stationary flow. The interaction of the exhaust gases with the catalyst will be studied with respect to different optimization goals. By reviewing similar studies and utilizing the acquired knowledge from passenger vehicles applications, while taking into consideration all the commercial vehicles' (CV) specific parameters, a design of experiment (DOE) will be created.

The remainder of this diploma thesis is divided into five sections covering the Chapters 2-6, respectively.

In Chapter 2, a turbocharger overview is presented along with the corresponding components and types. The basics of turbocharging are analyzed comprehensively, and the key characteristics explained in relation to the compressor and turbine maps. At the end of the chapter, the different control strategies are discussed with an emphasis on wastegates.

In Chapter 3, the design of experiment is realized. Based on available resources and internal experience, the simulation's parameters are decided for the stand-alone turbocharger model. The geometry preparation is shown and the meshing approach along with the mesh characteristics are outlined.

Chapter 4 is divided into three subchapters, each one featuring a case study. In Section 4.1, the grid Independence study is presented which evaluates the meshing strategy described in the previous chapter. Following the completion of the setup, in Section 4.2, a physical test is presented, and the turbine map is generated. The data are compared to the derived simulation values and the turbocharger evaluation is finalized. Two models are prepared to analyze the effect of the pipe length in obtaining realistic outputs. Finally, in Section 4.3, an in-depth examination of the wastegate opening angles and their effects on the turbocharger is conducted.

In Chapter 5, the aftertreatment is introduced. Based on literature review, a final model is prepared and explained before the assembly with the turbocharger. The final model, after examining different boundary conditions, is tested again in a variety of wastegate openings, followed by an investigation of the flow regime.

The conclusions of the thesis along with recommendations for future work are also presented in Chapter 6.

2. Turbochargers: Overview

Turbochargers are widely used in the automotive industry and play a crucial role in enhancing the performance and efficiency of internal combustion engines. Turbochargers are operating on the principles of exhaust gas energy recovery through the turbine which is then translated into kinetic energy that powers a compressor, feeding the engine's cylinders with compressed air. The introduction of compressed air significantly boosts engine power output without the need for a larger displacement engine by optimizing the air-fuel ratio and the overall combustion process. Turbocharging of ICEs has led to better packaging due to downsizing, reduction in weight, and overall improved fuel economy by reducing the specific fuel consumption.

In summary, the operation is as follows [Figure 1]:

The fuel is burned in the combustion chamber producing exhaust gases that pass through the exhaust manifold (5) during the cylinder's exhaust stroke. The hot gases enter the turbine housing through the inlet (6). The turbine wheel transforms the thermal and kinetic energy of the gases into mechanical energy by slowing them down resulting in a pressure and temperature drop (expansion). This kinetic energy is translated into the rotation of the connecting shaft driving the compressor wheel. The ambient air passes through an air filter before entering the compressor inlet (1). Inside the compressor, the air is sped up and forced into the volute which pressurizes it increasing its potential energy. The compressor discharge (2) is then redirected to the intercooler (3) which further increases its density by cooling it, while also increasing its resistance to detonation. Finally, the dense air enters the cylinders through the intake manifold (4).

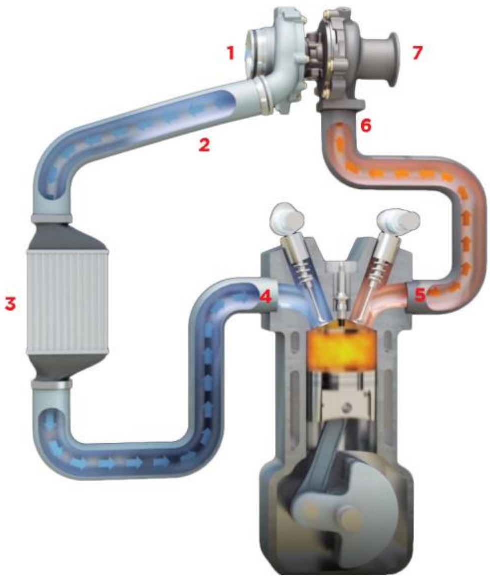

Figure 1 Turbocharger Operation [2]

To gain a better understanding of the effects of turbocharging, it is necessary to investigate the compression and expansion processes separately. For the sake of simplicity, an assumption is made that the internal processes in the turbine and compressor stages are described by adiabatic expansion and compression, respectively. Both processes occur in an open thermodynamic system without any heat exchange with the surroundings. This assumption is valid because of the flow character inside the volutes. As the processes happen very quickly compared to the time it takes for the gas to reach thermal equilibrium, the 1st Thermodynamic Law is applicable.

$$\dot{Q} - \dot{W}_x = \dot{m}\Delta h_0 \quad \text{with} \quad \dot{Q} = 0 \quad \text{leading to} \quad -\dot{W}_x = \dot{m}\Delta h_0$$

Eq. 1

For turbines that produce work the power is described as $P_t = \dot{W}_x$, whereas for compressors that absorb work the relation becomes $P_c = -\dot{W}_x$ [1].

In the realm of thermodynamics, fluid flow properties can be categorized into two primary groups: static and total (also known as stagnation). The concept of total fluid properties stems from the idea of isentropic flow deceleration, which, in line with Bernoulli's principle, corresponds to an increase in potential energy. In terms of enthalpy, this relationship can be expressed as follows [45]:

$$h_0 = h + \frac{1}{2} c^2$$

Eq. 2

Here, h_0 [J/(kg·K)] represents the total (or stagnation) specific enthalpy, h [J/(kg·K)] is the static specific enthalpy, and c [m/s] denotes the flow velocity with $\frac{1}{2}c^2$ describing the kinetic energy. Assuming also ideal gas properties the enthalpy h can be expressed as $h = C_p T$ and the equation 1 can be rewritten as:

$$-\dot{W}_x = \dot{m}[\mathrm{c_P} \Delta T + \frac{1}{2}(c_2^2 - c_1^2)] \approx \dot{m}\mathrm{c_P}\Delta T$$

Eq. 3

Furthermore, by utilizing the adiabatic isentropic relationship $\frac{p}{\rho^\gamma} = const$ [1] along with the ideal gas assumption, it is derived:

$$\frac{T_{02s}}{T_{01}} = \left(\frac{p_{02}}{p_{01}}\right)^{\frac{\gamma-1}{\gamma}}$$

Eq. 4

In Equations 3 and 4, ρ [kg/m³] represents the static density, γ [-] denotes the specific heat ratio (Poisson's constant) and cp [J/(kg·K)] represents the specific heat capacity at constant pressure.

In the case of real gases, the molecular size is not negligible, and they are not perfectly compressible. Additionally, latent heat is absorbed or released during phase changes. Hence, with real gases, specific gas constant R, specific heat ratio γ, and specific heat capacities c_P and c_V are generally functions of pressure (P) and temperature (T).

2.1 Compression Process

The ideal isentropic compression process 1-2s and the actual process 1-2 are shown in Figure 2. During the actual compression process from inlet 1 to outlet 2, the fluid experiences a pressure rise as it diffuses, which results in the transfer of kinetic energy to enthalpy. However, despite the pressure increase from inlet (P_{1c}) to outlet (P_{2c}), the total pressure decreases due to losses. The entropy of the actual compression process is higher as a portion of the kinetic energy is lost to turbulence and friction, which leads to a reduction in pressure recovery.

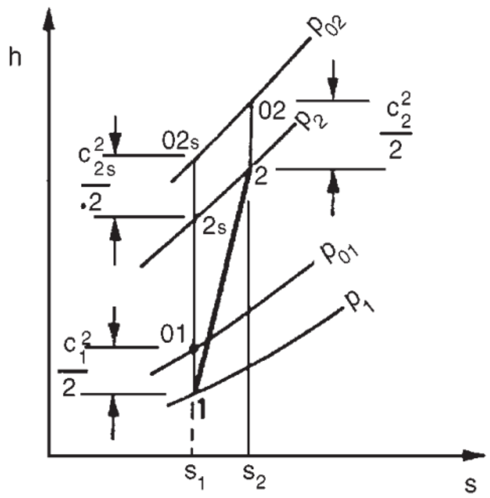

Figure 2 Diagram h-s for Actual vs Isentropic Compression [1]

Compressor total-total isentropic efficiency:

$$\eta_C = \frac{P_{Cs}}{P_C}$$

Eq. 5

In accordance with the equation 4, compressor efficiency η_c can be rewritten as:

$$\eta_c = \frac{T_{1c}\left[(PR_c)^{\frac{\gamma-1}{\gamma}} - 1\right]}{T_{2c} - T_{1c}}$$

Eq. 6

Compressor map

The compressor map [Figure 3] is a valuable graphical representation of the compressor's performance demonstrating the relationship between mass flow and pressure ratio in numerous operating conditions. The key characteristics of this map are:

1) Corrected mass flow rate $W_c = \dot{m}_c * \frac{\sqrt{T_{1c}/T_{ref}}}{P_{1c}/P_{ref}}$

Eq. 7

Where $\dot{m}_c = \frac{\text{kg}}{\text{s}}$ of air mass flow through the compressor (and engine)

2) Corrected turbo speed $N^* = \frac{N}{\sqrt{\frac{T_{1c}}{T_{ref}}}}$

Eq. 8

3)Compressor's pressure ratio $PR_c = \frac{P_{2c}}{P_{1c}}$

The compressor pressure ratio has a direct impact on engine performance, efficiency, and responsiveness, making it a key design parameter for turbochargers. It is essential for attaining the required power output at different altitudes, as well as for increasing fuel efficiency and preventing problems like knock.

The compressor map [Figure 3] is characterized by the surge and choke line, the turbo speed lines and the efficiency islands. Compressor maps' importance lies on the turbo matching.

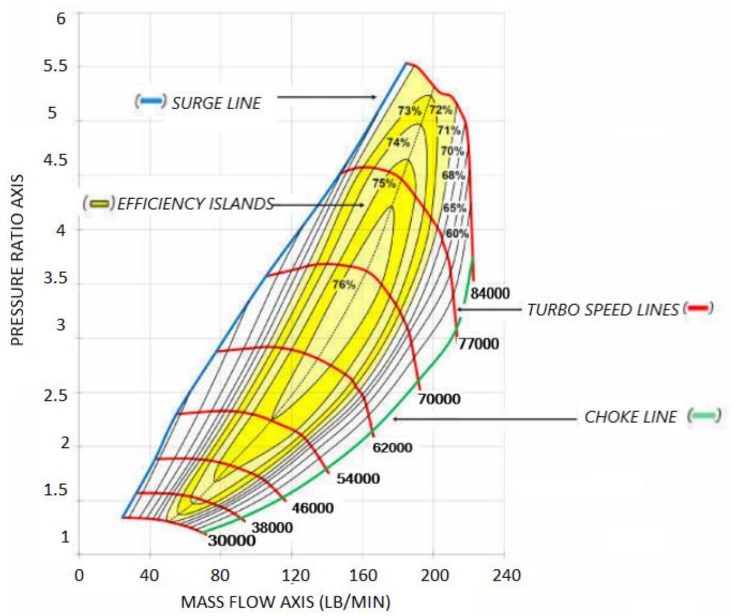

Figure 3 Compressor Map [3]

The surge line represents the leftmost threshold, that if surpassed, it leads to flow instabilities due to increased backpressure and essentially it means that the turbocharger is supplying the engine with more air than the engine can burn. Surge is a self-excited cyclic phenomenon usually caused by incorrect turbo matching or quick closing of the throttle during operation [19]. The surge limit can be widened by adding a wastegate or a by-pass valve to redirect intake pressure to the atmosphere and/or by incorporating a Ported Shroud compressor [Figure 4b] that recirculates a portion of the airflow before it enters the volute.

The choke line represents the rightmost boundary, and it typically symbolizes the area where efficiency has dropped below 58% and can be also expanded by having a shrouded housing [See Fig.4a] which allows the flow to bypass the throat and pass directly into the wheel.

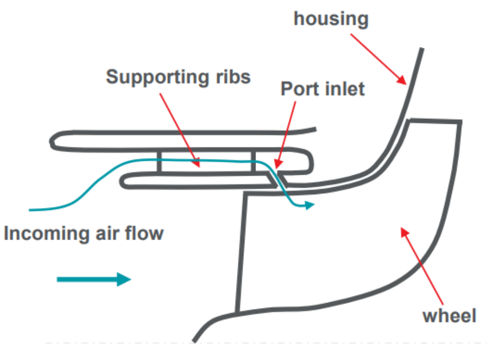

Figure 4a Ported Shroud: Bypassing flow [38]

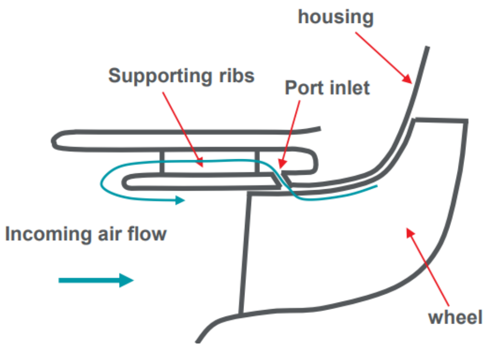

Figure 4b Ported Shroud: Recirculating Flow [38]

In the middle of the diagram there are concentric regions, called efficiency islands, which annotate the efficiency at any point. Approaching the limits, a notable decline in efficiency becomes evident while closer to the operational point, the efficiency peaks. The vertical lines are the turbo speed lines and as the speed increases the pressure ratio and/or mass flow will increase.

2.2 Expansion Process

Having briefly analyzed the turbine's working principle, a comparison between the isentropic expansion and the real expansion process can be seen in Figure 5. Due to a pressure loss caused by the exhaust after treatment systems, the outlet pressure (P_{2t}) is often higher than atmospheric, while the outlet temperature (T_{2t}) also increases following the increase of entropy.

Turbine efficiency in a single stage turbocharger is described by the total-to-static isentropic efficiency (η_{TS}) because the kinetic energy at the outlet is considered not useful:

$$\eta_{TS} = \frac{P_T}{P_{Ts}} = \frac{C_p(T_{1t} - T_{2t})}{C_p(T_{1t} - T_{2ts})} = \frac{(T_{1t} - T_{2t})}{T_{1t}\left(1 - \frac{1}{PR_T^{\frac{\gamma-1}{\gamma}}}\right)}$$

Eq. 9

Where $PR_T = \frac{P_{1t}}{P_{2t,static}}$

The expansion ratio PR_T relates the total Pressure at the inlet P_{1t} with the static Pressure at the outlet $P_{2t,static}$.

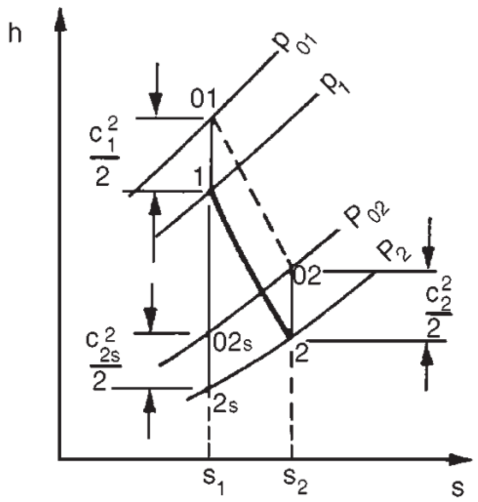

Figure 5 Diagram h-s Actual vs isentropic expansion [1]

However, the total-to-static turbine efficiency is an overestimation of the actual efficiency as it does not account for the losses. In a gas stand test, the measured outlet temperature is usually lower due to the internal flow irregularities, heat transfer through the housing and piping, etc. Another factor to consider are the losses in the power transfer from the turbine to the compressor due to mechanical parts like bearings and seals. All these additional losses [See Fig. 6] are translated into the mechanical efficiency of the turbine η_m that describes ratio of the actual compressor power P_C to the actual power produced by the turbine P_T.

Finally, the overall Turbine mechanical efficiency η_{TM} :

$$\eta_{TM} = \eta_{TS} * \eta_m \quad \textit{Eq. 1}$$

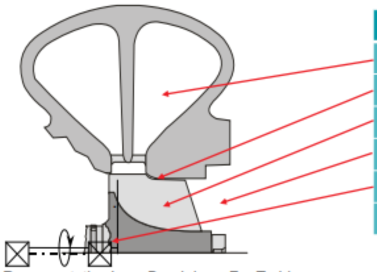

EFFICIENCY LOSS	POINTS
Housing or scroll	5
Tip clearance	3
Wheel blade channel	6
Exhaust kinetic energy	13
Bearings	2
Total	29

Figure 6 Loss Breakdown for typical Turbine [17]

2.2.1 Turbine map

Similar to a compressor map, a turbine map is a comprehensive graphical representation that illustrates the mass flow and efficiency characteristics of a turbine. Notably, in the case of turbines, the corrected mass flow and efficiency are depicted independently in relation to the pressure ratio of the turbine, although they are typically integrated into a single map. These turbine maps also include data on the corresponding compressor speeds, offering a comprehensive insight into the intricacies of turbocharger operations.

In Figure 7, a typical turbine map is presented. The upper lines represent corrected mass flow rates, while the lower lines depict efficiency values. Due to the centrifugal nature of the flow, it is evident that, especially in the case of radial turbines, as the rotational speed increases, the mass flow rate decreases at a constant pressure ratio.

Another significant consideration is that at a low PR_{TS} (meaning low rotor speed), turbine efficiency is relatively low. As the pressure ratio increases, efficiency also improves, peaking around the turbine's design point. As speed increases, losses are minimized, attributed to factors such as enhanced bearing lubrication due to elevated oil temperatures and the realization of the aerodynamic flow profile. However, beyond the design point, losses begin to rise once more [4,17].

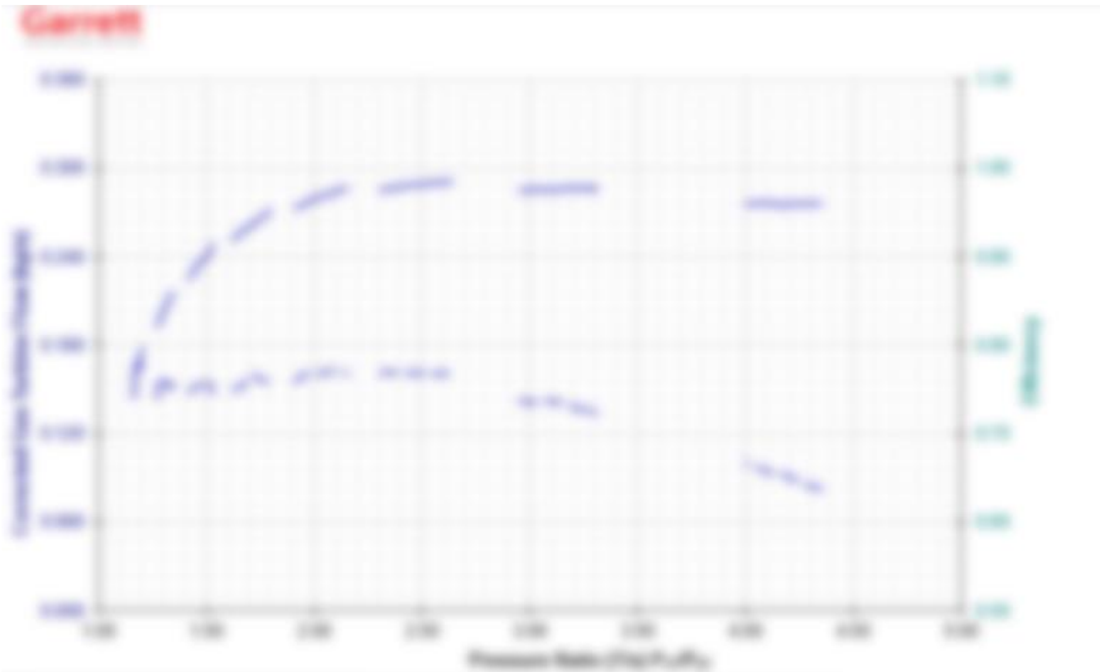

Figure 7 Turbine Map

The key characteristics of the map are:

1) Corrected turbine mass flow W_T :

$$W_t = \dot{m}_T * \frac{\sqrt{T_{1t}/T_{ref}}}{P_{1t}/P_{ref}}$$

Eq. 11

2) Corrected turbine speed

$$N^* = \frac{N}{\sqrt{T_{1t}/T_{ref}}}$$

Eq. 12

3) Turbine efficiency η_T

4) Turbine expansion Ratio $PR_T = \mathrm{P_{1t}/P_{2t}}$

2.3 Basic Components

To gain better understanding of this thesis' objectives, it is imperative to examine the operational conditions of a turbocharger. Turbochargers function within the demanding and harsh environments of modern diesel and gasoline engines. The turbine, in particular, is exposed to exceedingly high temperatures, reaching up to 1050°C in gasoline-powered vehicles. These temperatures are subject to cyclic fluctuations, contingent on engine speed and load variations. Consequently, the resulting differential thermal expansion and contraction impose significant stress on both the turbine housing and wheel, presenting considerable design challenges. This is especially pronounced when the turbine housing contains sections of varying thickness, as is the case with certain turbochargers, such as wastegated designs, rendering them susceptible to cracking. In this study, the focus is placed on diesel-connected turbochargers, where oxidative processes due to excess air play a pivotal role in potential failure mechanisms.

Elevated centrifugal forces acting on the turbine wheels, coupled with significant shear forces within the bearing, stem from the exceptionally high rotational speeds of the wheels, which can surpass 330,000 RPM. If these forces are not effectively managed, they may lead to shaft motion and subsequent wear on the bearings.

Further scrutiny of the turbocharger's operational environment reveals that the engine can introduce substantial vibrations. Turbochargers are engineered to accommodate vibrations of up to 25G (although a lower threshold applies to wastegated models). Additionally, the pressure differentials across the two wheels, arising from circumferential asymmetry, introduce an additional source of excitation for the turbine blades.

2.3.1 Compressor stage

The compressor stage is shown in detail in Figure 8. As discussed, ambient air will flow through the inlet to the compressor wheel (impeller) that is going to pressurize the air by forcing it to pass from a small passage called the diffuser. This pressurized air continues its diffusion as it progresses through the volute. The connection with the turbine stage is established through a shared shaft, which is supported by a bearing system.

These components, along with others, collectively constitute the Center Housing Rotating Assembly (CHRA).

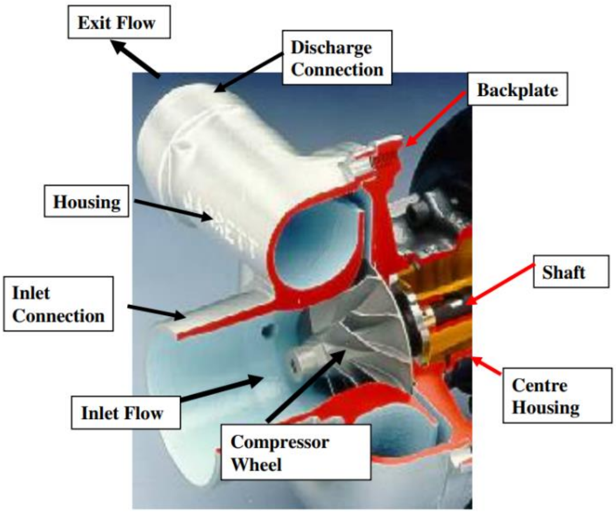

Figure 8 Compressor stage cut away view. [4]

A. Compressor Wheel

The compressor wheel must possess fatigue resistance, high strength, and a well-refined surface finish; thus, it is predominantly manufacture by titanium or aluminum alloys [5]. Based on Figure 9, it is observed that the compressor wheel comprises a central bore (1) surrounded by the nose (2). It consists of the main blade (3), the contour (4) and the leading and trailing edges (5,6) that finish at the tip or exducer (7), and in certain variations, these edges may be extended. Typically, a secondary blade known as the splitter blade (8) is also present. Each blade features a variable fillet (10) and is connected to the hub (9) area, with the rear side of the wheel referred to as Backwall.

Figure 9 Compressor Wheel Isometric view

B. Compressor Housing

The compressor housing is usually made of aluminum alloys although for certain commercial vehicles subject to elevated mechanical stresses, ferritic ductile irons may be employed.

Figure 10a provides a visual representation of the compressor housing's contour, the connections to the bearing housing, and the wall diffuser’s face. In Figure 10b, the image displays the inducer eye, the frontal view of the discharge, and the volute along with the inlet connection.

Figure 10a Compressor Housing Diffusor View

Figure 10b Compressor Housing Inlet View

There are several alternative compressor technologies, including the compressor ported shroud housing, fixed vane diffusers (as depicted in Figure 11) aimed at enhancing efficiency, variable inlet compressors, and two-stage compressors. These technologies can be encountered either individually or in combination, although they will not be subject to further analysis within the scope of this study.

Figure 11 Compressor Stage with Fixed Vanes [39]

2.3.2 Turbine stage

The primary components of the turbine stage comprise the turbine wheel and housing. The mounting flange is affixed to the manifold, facilitating the passage of exhaust gases. These gases traverse through the volute to the turbine wheel, where their velocity is reduced, converting their kinetic energy into mechanical energy to drive the shaft. Finally, the gases exit the housing through the diffuser.

A. Turbine Wheel

The turbine wheel, as illustrated in Figure 23a, due to the dismal operating conditions inside the turbine housing, must withstand high temperatures, while retaining excellent resistance to oxidation, fatigue, and creep. Additionally, a smooth surface finish is essential for aerodynamic efficiency. Typically, the turbine wheel is primarily fabricated from nickel-based super-alloys. Together with the shaft, these components form the shaft wheel assembly (SWA).

The turbine wheel's geometry plays a key role in the turbocharger's efficiency. Key wheel characteristics are the type based on flow, the contour, and the trim.

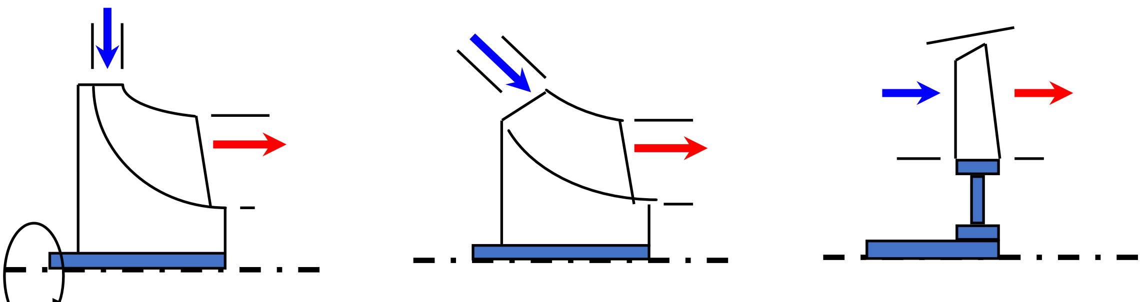

Figure 12a Radial *Figure 12b. Mixed-Flow* *Figure 12c. Axial*

There are three main types of turbine wheels. A typical automotive turbocharger employs a radial turbine [Figure 12a] with a radial compressor. However, various types of turbine wheels are available, depending on the specific application. In radial turbines, the airflow is introduced perpendicularly to the axis of rotation, resulting in reduced mechanical and thermal stresses for a given range, which ultimately enhances efficiency at higher speeds, as depicted in Figure 13. On the other hand, the mixed-flow wheel offers similar expansion capabilities but has a greater flow capacity compared to the radial design.

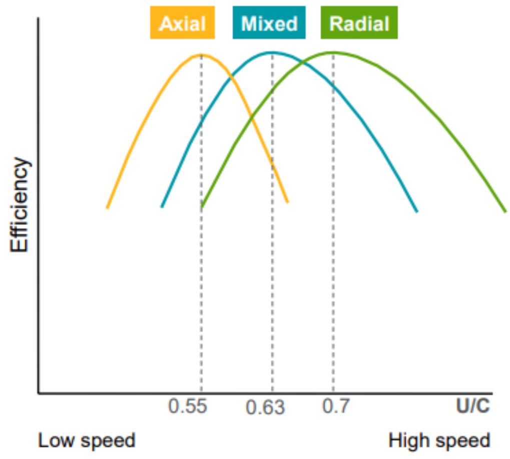

Figure 13 Efficiency vs BSR for different turbine wheel types [17]

Blade speed ratio is a measure of turbine load as it is a non-dimensional parameter which defines the ratio between the wheel tip speed versus the isentropic spouting velocity [Eq.13]. By increasing this parameter, the turbine load overall decreases. [6]

$$BSR = \frac{U}{C} = \frac{\pi \cdot \overline{D} \cdot \frac{N}{60}}{\sqrt{2 \cdot C_p \cdot T_{1t}\left(1 - \frac{1}{PR_T{}^{\frac{\gamma-1}{\gamma}}}\right)}}$$

Eq. 13

Where D is the mean flow diameter at the inlet and N is the turbine speed. Another wheel characteristic is the trim, which is defined as the ratio between the squares of the smaller to the larger diameter. For the turbine wheel the Exducer is the smallest one based on the air flow, so the trim is defined by [6,45]:

$$Trim = \left[\frac{D^2_{exducer}}{D^2_{inducer}}\right] * 100$$

Eq. 14

The trim is a measure of performance because with all other factors held constant, an increase of the wheel trim means an increase in flow capacity.

B. Turbine Housing

The turbine housing is mainly made from cast Irons or Stainless-Steel based materials depending on the application. [5]

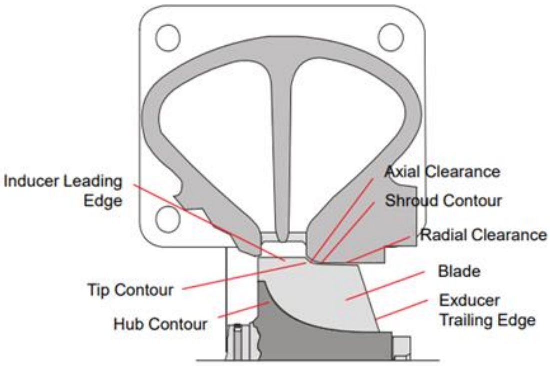

Figure 14 a. Turbine Housing Meridional View

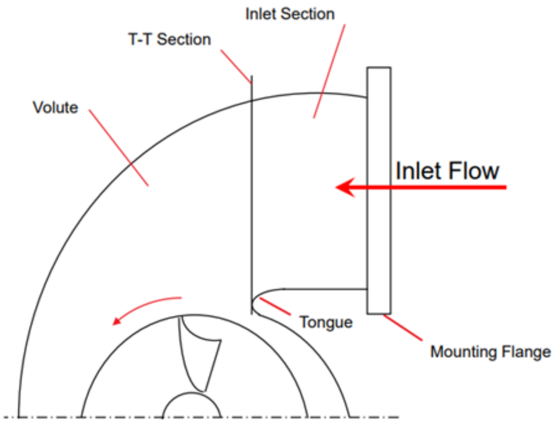

Figure 14 b. Turbine Housing Axial View

In Figure 14a, a meridional view of the turbine is observed. Along the flow direction, the inducer, its leading edge, the hub, and the shroud are encountered at the bottom and top, respectively. Notably, the clearances are visible, and they play a vital role in ensuring smooth turbine operation but should be kept at a minimum to achieve optimal aerodynamic performance. [17]

In the axial view, as shown in Figure 14b [17], the exhaust gases pass axially through the inlet section, which is surrounded by the mounting flange, before reaching the turbine wheel. The volute's design features a spiral shape that gradually tapers to redirect the flow and accelerate the gas.

Furthermore, the section separating the inlet and the volute is referred to as the T-T section and is located at the tongue which is described by the connection of the inlet lower surface with the volute’s tail end.

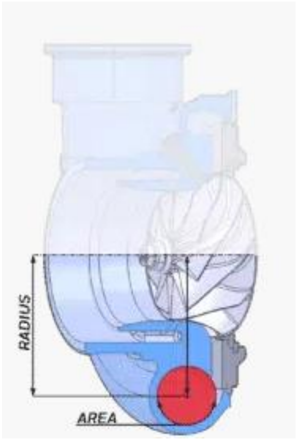

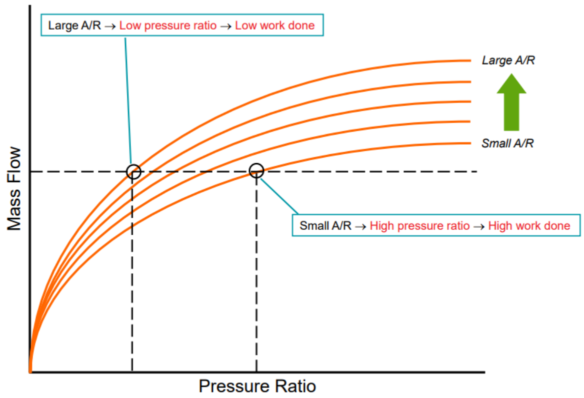

Figure 15 a. A/R Depiction [50]

Figure 15 b. Mass Flow vs PR graph with different A/Rs [17]

A significant attribute shared by both compressor and turbine housings is the A/R factor, which serves to define the size relationship of the gas passage. In the case of turbines, changes in the A/R, denoted as the cross-sectional area of the turbine inlet divided by the distance from the turbo centerline to the center of that area, are particularly influential. This is exemplified in Figure 15a.

With smaller A/R the turbine flow capacity decreases, resulting in higher backpressure. However, this reduction in area leads to an increase in gas velocity, ultimately leading to enhanced boosting power at lower engine speeds (rpms). Alternatively, a larger A/R allows for a greater volume of gas to enter the turbine, thereby reducing backpressure and generating increased power at higher engine speeds [Fig. 15b]. The choice of A/R is contingent upon the specific application, and for this model, the A/R values remain constant at [redacted] for the turbine and [redacted] for the compressor.

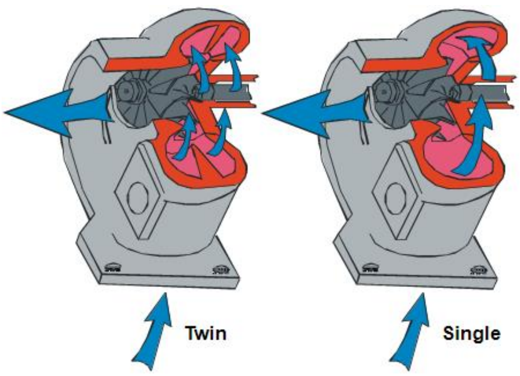

Figure 16 Twin Scroll and Single Scroll Turbo

Turbine housings can be primarily categorized based on the number of volutes they feature. Open turbine housings comprise a single volute, whereas twin-scroll turbochargers incorporate a divided turbine housing that leads to two independent flows, as depicted in Figure 16. Open-scroll turbos generally exhibit lower flow losses in comparison to their twin-scroll counterparts. However, their design limits their capacity to harness pressure waves to their advantage.

The primary advantage of twin-scroll housings lies in the separation of the exhaust gases by connecting different sets of cylinders in the corresponding opening based on the firing order. This division minimizes interference, preventing engine pulses from colliding and thereby reducing backpressure and unnecessary turbulence. Moreover, it results in more efficient utilization of exhaust gas energy, ultimately enhancing the turbocharger's performance.

While the bearing system and various other components play a crucial role in the turbo's operation, they will not be subject to further analysis within this paper.

2.4 Turbocharger Control

As mentioned previously in this chapter, packaging limitations have led to the development of turbocharger control technologies aimed at reducing the turbocharger's size while enabling it to function across a broader range of engine speeds, all while maintaining high efficiency. One such design is the free-float turbo, which represents a straightforward approach that heavily relies on the engine’s control strategy to maintain the required operating conditions and is mainly targeted for engines at constant speed.

By incorporating systems that regulate the exhaust gas flow through the turbine, the boost pressure is controlled resulting in an increased power and minimizing fuel consumption. Additionally, it protects the turbo and the engine from damage, shifting the limits discussed in the compressor map that correspond to the surge and choke phenomena. In Figure 17 below, a tree diagram categorizes these control strategies.

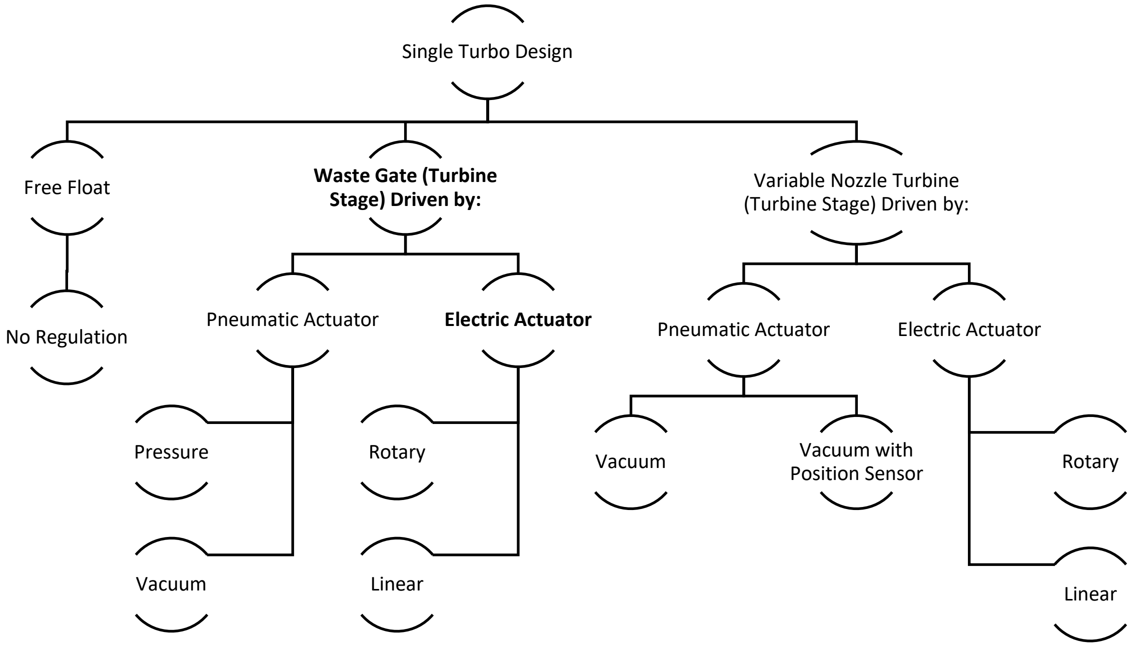

Figure 17 Division of the control strategies

The wastegate configuration consists of a by-pass valve, an arm, and an actuator assembly. As shown in Figures 18a., b., there are two types of wastegates, external and internal, with the latter being the most prevalent. The target is to allow for the use of smaller turbochargers that provide high efficiency in lower rpms, when the valve is closed, while simultaneously avoiding excess backpressure in higher rpms by redirecting the flow through the wastegate valve.

Due to emissions regulations, most vacuum pneumatic actuators have become outdated, and pneumatic actuators predominantly control the wastegate opening based on the rate of the integrated spring.

Electric actuators have an additional division: smart and simple. The turbocharger in question features an electric actuator with a smart control system that communicates with the vehicle's Engine Control Unit (ECU). This system can be strategically bypassed during cold starts to expedite the catalytic converter's activation.

Figure 18 a. Internal wastegate [41]

Figure 18 b. External wastegate [42]

The Variable Nozzle Turbine (VNT) is a geometric configuration that regulates boost pressure by altering the throat size of the turbine housing, as depicted in Figure 19a. This adjustment is achieved by tilting the vanes. It allows for the attainment of optimal pressure ratios without causing excessive backpressure and reduces turbo lag when compared to wastegate technology.

At lower engine speeds, the vanes are positioned in a way that increases the kinetic energy of the exhaust gases. In contrast, at higher engine speeds, the vanes are fully open to facilitate a higher flow capacity. This dynamic adjustment optimizes the turbocharger's performance across a range of operating conditions and is depicted in Figure 19b.

Figure 19 a. Cut-away View of a VNT Turbocharger [43]

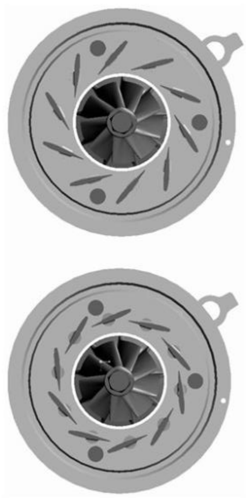

Figure 19 b. Vanes' Opening and Closing [44]

3. Setup of Turbine Stage Simulation

The simulation of the flow through the turbine was conducted by utilizing Computational Fluid Dynamics software, and more specifically ANSYS CFX. This software allows for a cost-effective detailed study of the complex flow phenomena, providing valuable insights regarding the turbocharger behavior. Various studies [36,44,47,48] followed the three-dimensional approach to simulate the complex turbulent flow inside a turbocharger. The setup was carefully decided and tested to obtain realistic results and will be further discussed throughout this chapter. Finally, the geometry preparation was carried out using CatiaV5 software.

3.1 Governing equations

Every computational method is based on the fundamental laws of conservation of mass, momentum, and energy to describe the behavior of a fluid flow. The finite volume method's differential equations to be solved are the transformed Lagrangian forms of the physical laws using the Reynolds Transport theorem and then converted to volume integrals using Gauss' Divergence Theorem. Assuming x represents a property associated with the fluid where:

$$X = \iiint_{\Omega} \rho x \ d\Omega$$

Eq. 15

Then, the Lagrangian derivative is related to the Eulerian control volume by the application of Reynolds Transport theorem:

$$\frac{dX}{dt} = \iiint_{\Omega} \frac{\partial(\rho x)}{\partial t} + \oiint_{A} x(\rho\vec{u}\cdot\hat{n})dA$$

Eq. 16

The conversion of the surface integral into a volume integral is achieved through the use of the Divergence Theorem, resulting in:

$$\frac{dX}{dt} = \iiint_{\Omega} \frac{\partial(\rho x)}{\partial t} + \iiint_{\Omega} \nabla \cdot \vec{u} d\Omega$$

Eq. 17

1) Continuity equation

For a finite volume, the net mass that crosses the system boundary must be balanced, meaning the rate of change of mass within is equal to the rate of mass exchange.

$$\frac{dM}{dt} = 0 \ \rightarrow \frac{\partial \rho}{\partial t} + \nabla \cdot \rho \vec{u} = 0$$

Eq. 18

2) Momentum equation

The momentum equation is another form of Newton's second law of motion, stating that the change in momentum is a resultant of diffusion, convection, friction, and all additional forces applied to the fluid on the surface of the control volume and internally. For a more in detail approach refer to [8].

$$\rho \left[\frac{\partial \vec{u}}{\partial t} + \vec{u} \cdot \nabla \vec{u}\right] = -\nabla p + \nabla \cdot \bar{\bar{\tau}} + \rho \vec{g} + \vec{F}$$

Eq. 19

Where the $\bar{\bar{\tau}}$ are the viscous stresses, proportional to the rates of deformation, $\rho \vec{g}$ the gravitational and $\vec{F}$ the external body forces (especially important for the following porous media modelling).

3) Conservation of energy

This equation is derived from the First Law of Thermodynamics and encompasses all aspects of work and energy, both within the system and at its boundaries. The term E represents the total energy, comprising internal, kinetic, and potential energy within the system [9].

$$\frac{dE}{dt} + \nabla \cdot [\vec{u}(E+p)] = \nabla \cdot [k\nabla T + (\bar{\bar{\tau}} \cdot \vec{u})] + \dot{S}g$$

Eq. 20

In the above equation the generation term $\dot{S}g$ represents the change of the total energy by heat sources like radiation, reaction, etc.

These governing differential equations, also known as Navier-Stokes equations, along with appropriate initial and boundary conditions, provide a solid mathematical framework for fluid simulations. In addition, equations of fluid state, turbulence and many more problem-specific relations can be added to the solution.

3.2 Basic of turbulence equations

Throughout this research, the turbulence will be modeled using the Reynolds-Averaged Navier-Stokes (RANS) approach. This technique requires a significantly coarser grid to model the flow than LES and DNS, while it enables us to consider the flow's stationary (Steady state) solutions. Considering Reynold's decomposition the local velocity for each point can be rewritten as the sum of the fluctuating and average velocity terms : $u = \overline{u} + u'$ and it canbe generalized for other scalar quantities as $\varphi = \overline{\varphi} + \varphi'$

By substituting this decomposition to the mass and momentum equation the RANS equations are produced:

$$\frac{\partial \rho}{\partial t} + \frac{\partial}{\partial x_i}(\rho u_i) = 0$$

Eq. 21

$$\frac{\partial}{\partial t}(\rho u_i) + \frac{\partial}{\partial x_j}(\rho u_i u_j) = -\frac{\partial p}{\partial x_i} + \frac{\partial}{\partial x_j}\left[\mu\left(\frac{\partial u_i}{\partial x_j} + \frac{\partial u_j}{\partial x_i} - \frac{2}{3}\delta_{ij}\frac{\partial u_l}{\partial x_l}\right)\right] + \frac{\partial}{\partial x_j}(-\rho u_i' u_j')$$

Eq. 22

Where I is the unit tensor and $-\rho \overline{u_i' u_j'}$ the Reynold's stresses that represent turbulence. The Boussinesq [10] assumption is most commonly used which correlates these stresses to the mean velocity gradients:

$$-\rho \overline{u_i' u_j'} = \mu_t \left(\frac{\partial u_i}{\partial x_j} + \frac{\partial u_j}{\partial x_i} \right) - \frac{2}{3} \left(\rho k + \mu_t \frac{\partial u_k}{\partial x_k} \right) \delta_{ij}$$

Eq. 23

In Equation 23, k symbolizes the turbulent kinetic energy with

$$k = \frac{1}{2} (\bar{u}'^2 + \bar{v}'^2 + \bar{w}'^2)$$

Eq. 24

and only appears in the equation when $i = j$.

The eddy diffusivity Γ_t is described by the Equation 25 ,as follows:

$$-\rho u_i' \phi' = \Gamma_t \frac{\partial \phi}{\partial x_i}$$

Eq. 25

and it can be then connected with the turbulent viscosity μ_t by introducing the Prandtl/Schmidt numer :

$$\sigma_t = \frac{\Gamma_t}{\mu_t}$$

Eq. 26

3.3 Problem Statement

The objective of this thesis is to focus on the performance analysis and optimization of the THS-Aftertreatment system. For this reason, the turbocharger is considered to operate under relatively steady conditions during normal operation, thereby becoming a Steady-State problem. In this process, gases enter the volute inlets, pass through the rotating wheel, and subsequently exit the housing through the outlet. Simultaneously, a portion of these gases is diverted from the diffuser and exits through the wastegate. The essential characteristics of both the engine and the turbine are outlined in Table 1.

Table 1 Key characteristics of the application

Engine Capacity	**12.74 [L]**
Engine Max. Power @1800 rpm	[redacted] **[kW],** [redacted] **[HP]**
Engine Max. Torque	[redacted] **[Nm] @** [redacted] **Rpm**
Number of Cylinders	**6**
Turbocharger system	**1-stage, fixed geometry, twin-scroll**
Turbine blade number	[redacted]
Turbine wheel OD	[redacted] **[mm]**
Turbine wheel ID	[redacted] **[mm]**
Turbine housing A/R	[redacted]
Wastegate Valve Diameter	[redacted] **[mm]**

The turbine housing system contains a moving wheel inside a stationary housing, with the interface between the zones being nearly uniform. Given that a steady-state problem involving multiple zones is addressed, the Multiple Rotating Reference Frame method is selected. The model is divided in multiple domains, where rotational or stationary frame equations are applied depending on the domain nature, and interfaces that separate these zones. There are two approaches on how to treat these equations at the interface: Multiple Reference Frame and Sliding Mesh Model.

For this application, the MRF model, and more specifically the Mixing Plane Model (MPM), was chosen as it provides accurate results [20] with less computational expense compared to transient simulations. In this model, the domains are considered as steady state problems and at the interfaces Volute-Wheel and Wheel-Outlet, flow field data are transmitted as boundary conditions respectively and are then mixed out, allowing for the elimination of any unsteadiness, thus yielding a steady-state result.

3.4 Domains

The approach followed is the simulation of the rotating region around the wheel and the uniform flow through the two volutes- the inlet of the turbine housing and the outlet.

Table 2 Volute Domain

Domain	Boundary surface	Boundary type	Details
Volute	Volute Inlet	Inlet	Subsonic Flow, Total Pressure (p1t) along with total temperature (T1t), medium intensity Turbulence
	Interface Volute - Wheel [Side 1]	Interface	Conservative Interface flux for Mass and Momentum, Turbulence and Heat Transfer
	Interface Volute - Wastegate [Side 1]	Interface	Smooth Wall with Conservative Interface Flux for Heat Transfer
	Volute Wall	Wall	Smooth, No slip Wall, Adiabatic

Table 3 Wheel Domain

Wheel	Interface Wheel-Volute [Side 2]	Interface	Conservative Interface flux for Mass and Momentum, Turbulence and Heat Transfer
	Interface Wheel Periodicity [Side 1]	Interface	Conservative Interface flux for Mass and Momentum, Turbulence and Heat Transfer
	Interface Wheel Periodicity [Side 2]	Interface	Conservative Interface flux for Mass and Momentum, Turbulence and Heat Transfer
	Interface Wheel-Outlet [Side 1]	Interface	Conservative Interface flux for Mass and Momentum, Turbulence and Heat Transfer
	Wheel Blade	Rotating Wall	Smooth, No slip Wall, Adiabatic
	Wheel Hub	Rotating Wall	Smooth, No slip Wall, Adiabatic
	Wheel Shroud	Counter-Rotating Wall	Smooth, No slip Wall, Adiabatic, with wall velocity

Table 4 Outlet Domain

Outlet	Outlet	Outlet	Subsonic Flow, Average Static Pressure (p2t) over the whole outlet with 0.05 blend
	Outlet Valve	Wall	Smooth, No slip Wall, Adiabatic
	Outlet Wall	Wall	Smooth, No slip Wall, Adiabatic
	Outlet Wheel Nose	Rotating Wall	Smooth, No slip Wall, Adiabatic, with wall angular velocity rotating around Global Z axis
	Interface Outlet-Wheel [Side 2]	Interface	Conservative Interface flux for Mass and Momentum, Turbulence and Heat Transfer
	Interface Outlet - Wastegate [Side 2]	Interface	Smooth Wall with Conservative Interface Flux for Heat Transfer

For the purpose of this research, the walls are modelled as adiabatic for simplification. Usually, thermal loads are calculated and quantified during the design process but since the aim is to analyze the exhaust flow in an already finalized model, it is assumed that no heat exits through the walls. Studies have shown that the adiabatic assumption produces better results at lower speeds [11].

This simplification is valid since the changes in temperature happen so rapidly before the fluid reaches thermal equilibrium and the temperature differences are so high that it is safe to assume the heat transfer is close to zero for this type of simulation. The walls were modelled as smooth due to the actual roughness being very small and not easily quantifiable and that helps, also, to prevent an unnecessary shift in the y+ by the software's treatment method near rough walls.

Regarding the impeller, Single Blade Passage (SBP), as well as the Full Turbine (FT) are the dominant approaches. In the former, the flow inside one passage of the blade is simulated, and the set periodic surfaces are representative of the rest of the domain [21]. Although the preparation of the geometry is more tedious, the simulation time is significantly reduced, while still providing accurate results deeming it the best option considering the needs of this research.

Table 5 List of Interfaces-Turbocharger

Interface	Interface Type	Mesh Connection	Details
Volute - wheel	Fluid - Fluid	GGI	Stage (Mixing Plane) with downstream stage average velocity constraint and pitch angle 360° for the volute and 360°/# of blades for the wheel due to pie sectioning
Wastegate [Volute-Outlet]	Fluid- Fluid	GGI	General Connection interface, with no slip wall if WG is closed or mass and momentum conservative flux if opened.
Wheel Periodicity	Fluid- Fluid	Automatic	Rotational Periodicity around Global Z axis
Wheel - Outlet	Fluid- Fluid	GGI	See Volute-Wheel Interface (with Outlet instead of Volute)

3.5 Turbulence Model

The Shear Stress Transport turbulence mode was selected for this simulation, based on extensive validation from Garret's internal research studies available to the author, and relevant independent publications that deem this method the most accurate model for aerodynamic simulations. [12, 13]

In general, the SST model developed by Menter [14] is a hybrid approach that combines the accurate formulation of the *k-ω* model near the wall with the free-stream independence of the *k-ε* in the bulk flow. Both base models are multiplied by a blending function that activates the corresponding model based on wall distance and then added together. The constants and definition of turbulent viscosity are modified while a cross-diffusion term is introduced to ensure appropriate behavior throughout the zones, more analytically explained in [22].

$$\frac{\partial}{\partial t}(\rho k) + \frac{\partial}{\partial x_i}(\rho k u_i) = \frac{\partial}{\partial x_j}\left(\Gamma_k \frac{\partial k}{\partial x_j}\right) + \tilde{G}_k - Y_k + S_k$$

Eq. 27

$$\frac{\partial}{\partial t}(\rho \omega) + \frac{\partial}{\partial x_i}(\rho \omega u_i) = \frac{\partial}{\partial x_j}\left(\Gamma_\omega \frac{\partial \omega}{\partial x_j}\right) + G_\omega - Y_\omega + D_\omega + S_\omega$$

Eq. 28

Where $\tilde{G}_k$ and $\tilde{G}_\omega$ represent the generations of turbulence kinetic energy k and specific dissipation rate ω.Similarly, Γ_k and Γ_ω are the effective diffusivities while Y_k and Y_ω are the dissipation due to turbulence. Lastly, D_ω symbolizes the cross-diffusion term and S_k and S_ω are source terms, user specific. For all the fluid models the turbulence intensity was set to 5%.

3.6 Solver Type

There are two ways to solve the discretized equations, segregated or coupled. ANSYS CFX uses a pressure based coupled solver, which solves the momentum and pressure equations simultaneously by incorporating the pressure correction within the momentum step. A similar study about the catalyst-turbocharger behavior was conducted that proved that coupled solver converged the majority of times and the difference between the two solvers were less than 1% for normal flow conditions [23].

3.7 Convergence Parameters

A closed wastegate model with initial conditions P_{1t}= [redacted], T_{1t}=[redacted] , P_{2t}= [redacted] was evaluated to find the number of iterations for convergence. This model was verified prior to the convergence study, and it was utilized to define the number of iterations that is sufficient for this research. Throughout this thesis, the following requirements were employed to monitor solver convergence:

[redacted]

- [redacted]

The high-resolution Advection Scheme and Turbulence Numerics were selected.

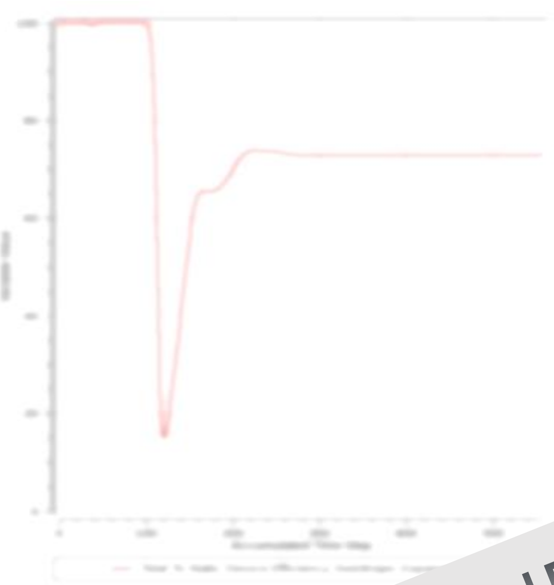

Figure 20 a. Total t

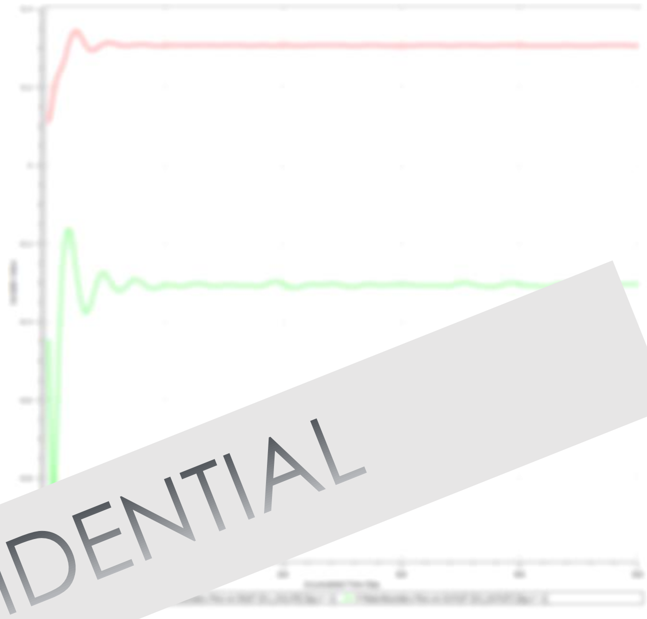

Figure 20 b. Mass Flow Monitors vs Time Step

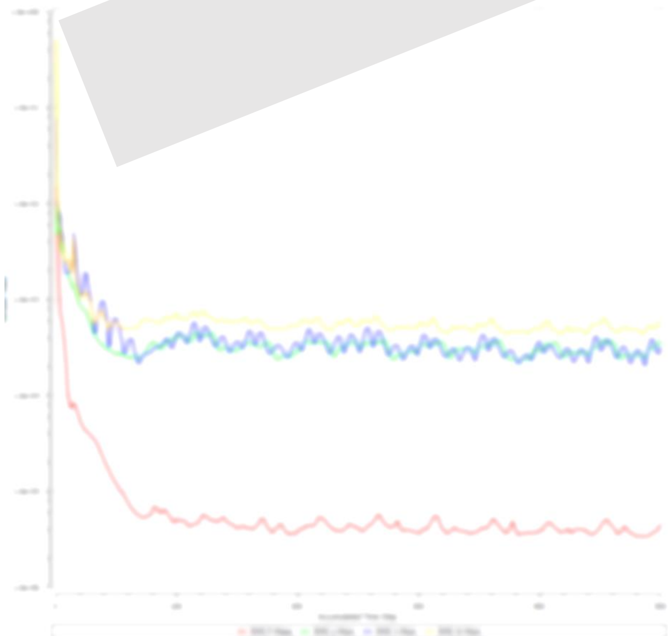

Figure 20 c. RMS Residuals vs Time Step

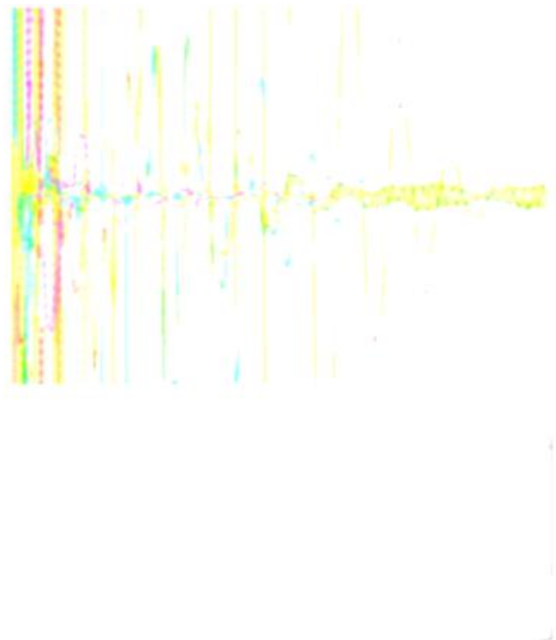

Figure 20 d. Imbalances vs Time Step

3.8 Geometry Preparation

Figure 21 [redacted] Turbocharger assembly

The geometry of the wheel nose and the incorporation of twin-scroll technology posed certain challenges during the model preparation, particularly in dividing the three main sections. The first required action for preparation of the 3D model is the cleanup of insignificant features (p. ex the engraving in the housing) and update of the turbine wheel. The fluid domain of the turbine wheel constitutes a pie-shaped sector of the entire wheel, encompassing a single blade. This sector is further divided into nine subcategories, which will be elaborated upon in the subsequent subchapter dedicated to the wheel domain.

Figure 22 a. CAD Isometric View

Figure 22 b. Turbine Outlet View

The 3D model was first inserted in CATIA V5, as a complete assembly, and after cleaning up the CAD it was ready for wheel redesign. The redesign aimed to achieve a better-quality mesh and to simplify the result. [redacted]

[redacted] Moreover, the variable fillets around the blades were replaced by constant fillets, keeping the geometry relatively simple for the pie sector generation.

Figure 23 a. Original Turbine heel

Figure 23 b. Turbine wheel after preparation

After the turbine wheel was prepared separately, it was inserted as a Shaft-Wheel Assembly (SWA). This was done to ensure proper placement and alignment with the housing in accordance with the drawing specifications. The machining of the wheel was carefully removed to allow the small clearance needed for realistic operating conditions, and the contour was cut out in accordance with the tolerances. The shaft, which was not needed for the simulation, was excluded from the finalized model.

The next step was to close any small gaps specifically between the Valve Arm and the opening [Figure 24]. As a first approach the gaps were sealed by simple cylinders to ensure airtight connection and any unnecessary parts like washers were removed.

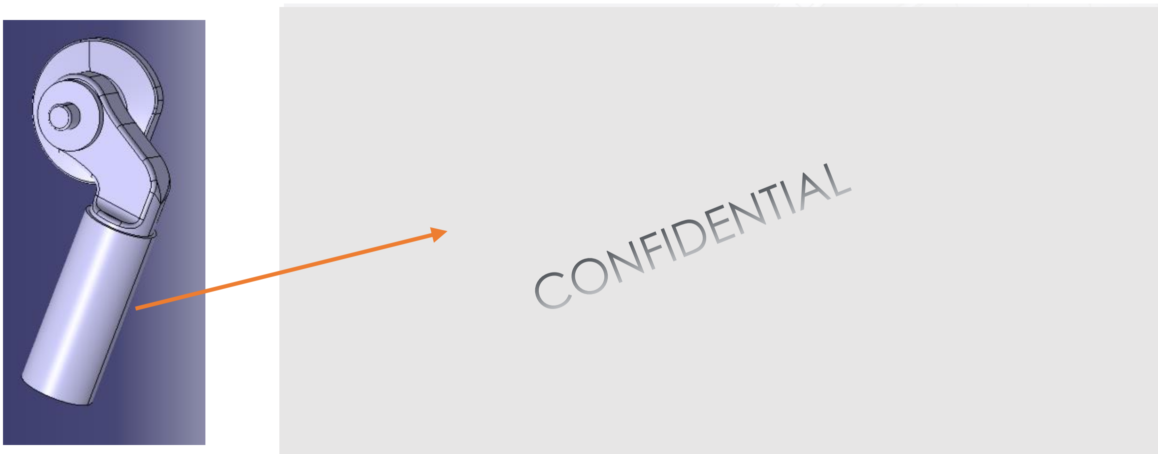

Figure 24 Close-up of gap elimination

Then a CAT Part was generated from the product, marking the initiation of the primary preparation process. The rotation axis was set as the Z-axis with the direction of the flow through the outlet following “plus Z” coordinates and the flow passage cross section located at tongue (TT section) passes the YZ plane, as shown below.

Figure 25 Orientation of the model

3.8.1 Fluid Domains

Volute

Figure 26 Before and after of the Volute domain preparation

The volute fluid domain [Fig. 26], was created by extracting all the internal surfaces of the THS Volute and comprises of the volute wall, inlets, tongue, outlet and wastegate interface. The reason for defining the tongue is for easier mesh refinement of this area in the pre-processing step and the interface with the wastegate is defined to indicate if mass and momentum transfer take place, depending on the wastegate position**.** Lastly, the volute outlet serves as the interface between the volute and wheel, which is defined by cutting the volute with a cylinder slightly bigger than the wheel's diameter, and it is shown in Figure 27.

Figure 27 Contact zone of Wheel patch and Volute.

Turbine Wheel

The wheel was approached differently, due to the pie sectioning method. Initially, two surfaces were defined: Surface 1, which indicated the point where the wheel ended just before the shaft, and Surface 2, which divided the wheel nose in half. On one side, Surface 2 marked the end of the pie sector, and on the other side, it defined the inlet of the Outlet domain.

Following the extraction of these surfaces from the wheel, a wheel domain was established by dividing the wheel with the aforementioned surfaces and a cylinder representing the contact between the wheel and the volute, as shown in Figure 28, step 1. This process resulted in the geometry shown in step 2.

Then, surfaces were created by using spline-based surfaces that were rotated to encompass a single blade, and the final part was split.

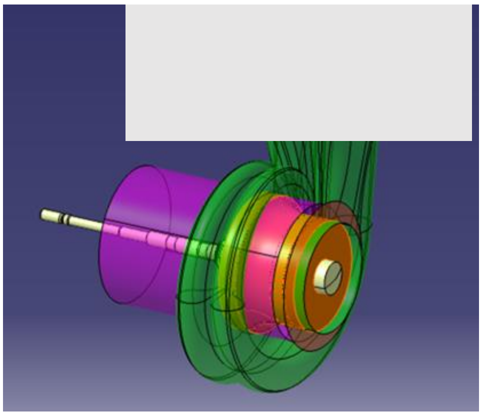

Step 1: Enclosing the area of interest.

Step 2: Splitting the main geometry.

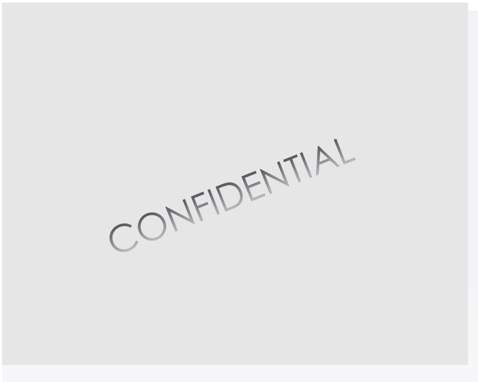

Step 3: Creating the Pie section.

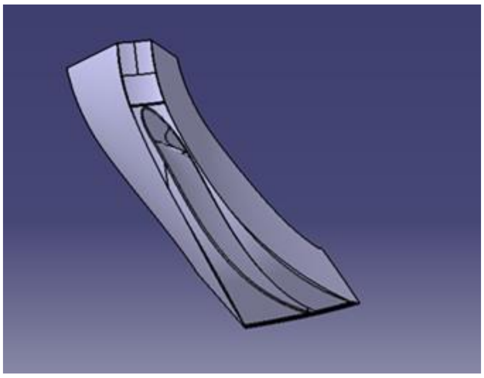

Step 4: Final wheel domain.

Figure 28 Step by Step of the wheel domain creation

The wheel was divided in 9 sections, the wheel inlet, shroud, shroud side , side 1 and 2 , hub, blade and blade top and finally wheel outlet. The division was helpful not only for independent mesh refinement, but also for defining the boundary conditions more precisely, and can be shown below:

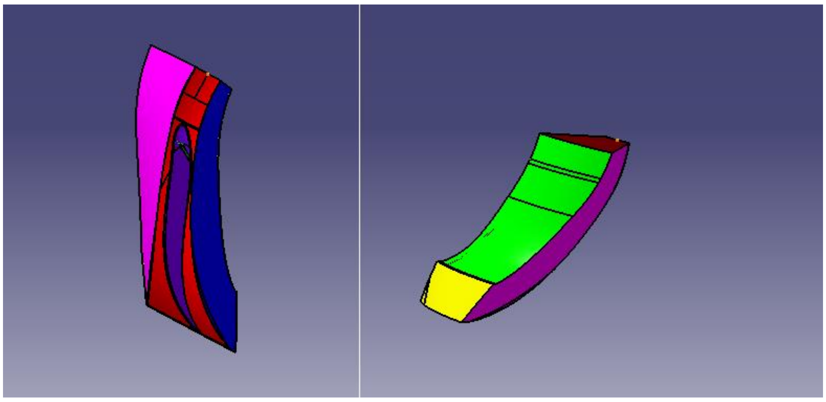

Figure 29 Wheel's color-coded regions

Outlet

The outlet fluid domain demanded special attention due to [redacted], as illustrated below. [redacted] creating disturbances in the main flow. These disturbances and their effects will be discussed in detail during the post-processing stage of the analysis.

Figure 30 a. Diffuser Front View *Figure 30 b. Diffuser Side View*

The outlet domain included the contact region, as shown in Figure 31a, where a portion of the wheel nose is visible. Then, the interface with the Volute was split as mentioned above, and an extention was made to capture the flow using a parametric design method, making it easily adjustable to the desired length. This extension will undergo further analysis in section 3.8.2.

Figure 31 a. Contact region of Diffuser Inlet and wheel

Figure 31 b. Contact region between Volute and Diffuser (WG representation)

The decision was made to incorporate the wastegate as part of the Volute fluid domain, so that it can function as an obstruction to the fluid flow. The valve's surfaces were extracted and then the geometry was split [Fig. 32b]. To manipulate the angle of the valve without requiring a redesign, a rotational equation was introduced between the valve and the outlet wall, as shown in Figure 32a. This approach allows for control of the valve angle to affect the flow through the wastegate, without the need for significant geometric changes.

Figure 32 a. Opening Angle of 10^o *Figure 32 b. View of the split Valve enclosed in the channel.*

In Figure 33, all the sub-domains can be seen with their corresponding color for better visualisation: Red: Outlet ,Yellow: Interface wheel-outlet ,Green: Wheel nose ,Blue: Valve ,Magenta: Interface Volute-Outlet

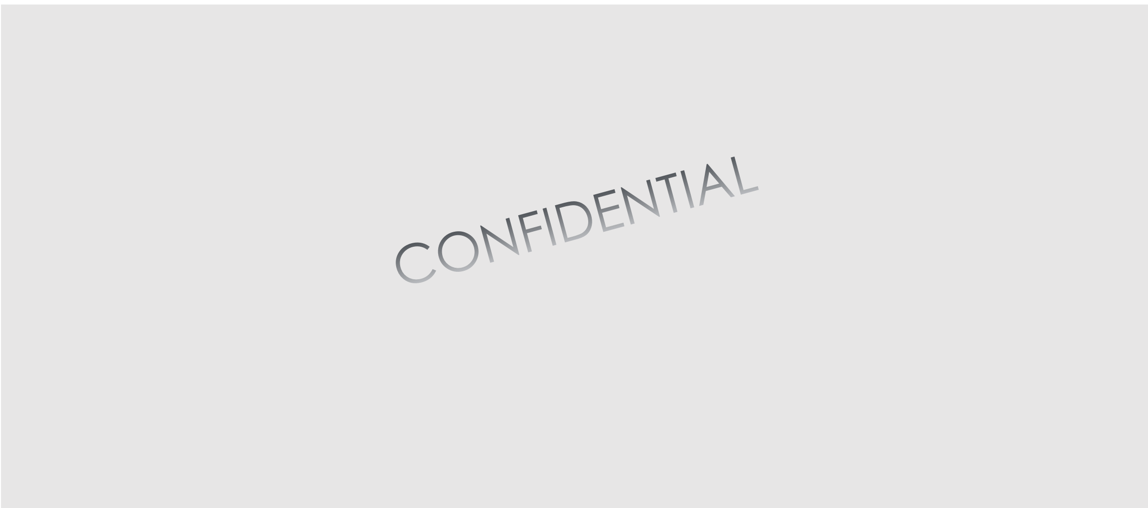

Figure 33 Color-coded Diffuser's Subdomains

3.8.2 Inlet and outlet surfaces extension

In the following short study, different lengths of outlet extensions were examined to assess differences in measured data and flow patterns. The ultimate goal was to determine a suitable extension length that achieves the desired results without exceeding the allowable pipe length threshold for the aftertreatment packaging, which will be further analyzed.

Extending the geometry's inlets and outlets before starting a simulation has a few key advantages. The aim behind this modification is for the flow to be fully realized while also eliminating the risk of reverse flow. Fully developped flow is key as the entrance and outflow areas should have a consistent velocity profile to aid in numerical convergence and produce more precise findings.

It is essential to make sure the outlet boundary condition is positioned far enough downstream at steep curves, especially given the angles of the diffuser geometry. Otherwise, the simulation may diverge and yield inaccurate results, due to unwanted flow recirculation that can lead to divergence.

The following cases were examined with extensions on both the entrance and exit of the flow. Particularly, the flow at the volute's inlet was realized quicker, due to the nature of the regime so in the following Figures, focus was given at the diffuser's outlet region. The volute extensions was decided to be approximately 100mm . For simplification, the interface between the Volute and Outlet was modeled as a wall, to indicate that the bypass valve was closed, and the extensions were correlated with the diameter of the Shaft-Wheel Assembly (SWA).

The inputs for this model were based on standard testing , and convergence was reached after Case 3.

CASE 1

The following model represents the real turbocharger without any extensions. Severe flow recirculation can be observed as the fluid enters the wastegate channel from both sides. The results this model yieds are unrealistic and extensions need to be made.

Figure 34 Velocity Vectors (left) and 3d streamlines (right) of No extension Model.

CASE 2

In this model the outlet extension was set to 86 mm [redacted] and the split inlet was extended by 50mm. While this extension resolved partially the recirculation issue, it is evident that there is a notable stagnation point in the primary flow (indicated by the dark blue area), which divides the flow into two distinct regions, [redacted]. Flow separation can also be observed at [redacted]. As a result, it is concluded that further extension is required to optimize the flow patterns and eliminate these issues.

Figure 35 Velocity Vectors (left) and 3d streamlines (right) of 86mm extension Model.

CASE 3

The inlet was further extended, reaching 100mm, which proved to be adequate for the simulation as further extension did not significantly impact the incoming flow. Additionally, the diffuser extension was doubled, and the outputs were deemed satisfactory. As expected turbulence is present, and the geometry of the diffuser [redacted]. For the most part, the main flow is realized with some small vorticities still present. The results that the model yielded were within range of the testing, which will be further discussed in the next chapter.

Figure 36 Velocity Vectors (left) and 3d streamlines (right) of 175mm extension Model.

CASE 4

In this case, the extension length is tripled in comparison with Case 2. Similar behavior is observed in the previous case with the flow attaching more to the walls. This is partially due to the recirculation at the [redacted], which was previously observed but is more evident in the top model of Figure 37. The results did not show a substantial difference compared to Case 3 ,and considering the computational time, the setups that follow were tested preliminary with the extensions as described in the third case.

Figure 37 Velocity Vectors (top) and 3d streamlines (bottom) of 260mm extension Model.

3. 9 Meshing

Each component with its corresponding sub-components was meshed individually to ensure appropriate meshing that realistically captures the geometric features and the y+ target is successfully reached. The quality criteria were set to be a Minimum Face angle of 20^{o} with a Maximum of 160^{o} and a Minimum Volume of zero. The total element number was 12.247.322 with a global mesh of 0.007 m and local body sizing as shown in the table:

Volute

Table 6 Volute Mesh

Object	*WALL*	*TONGUE*	*OUTLET*
Type	Factor of Global Size	Element Size	Factor of Global Size
Element Size Factor			
Element Size			
Defeature Size Factor			
Global Size Factor			
Capture curvature		CONFIDENTIAL	
Curvature Normal Angle			
Curvature Min Size Factor			

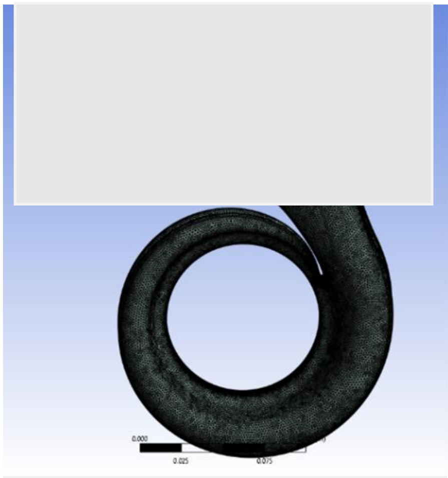

Figure 38 a. Side view of the Volute with Visible Mesh

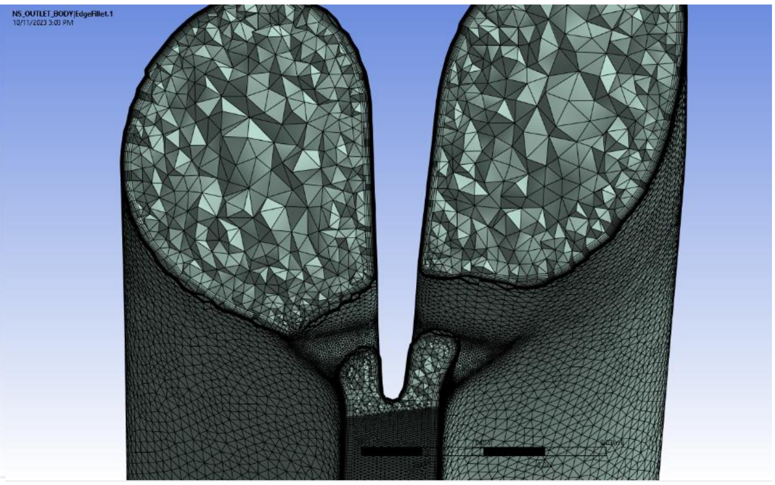

Figure 38 b. Volute mesh in Section Cut View

The meshing of the volute, along with the sizing of distinct areas, can be observed in Figures 38a and 38b. The mesh was conducted in accordance with the Table 6. Specifically for the tongue, defeature size was set to [redacted] m. Boundary layers are clearly visible, as are the tetrahedral elements at the center. The sized-down tongue region is also clear at the section cut view.

Wheel

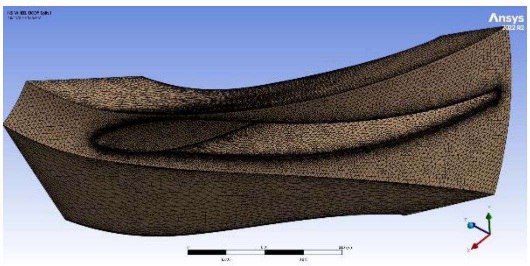

Figure 39 a. Close-up of the wheel's mesh (Blade side)

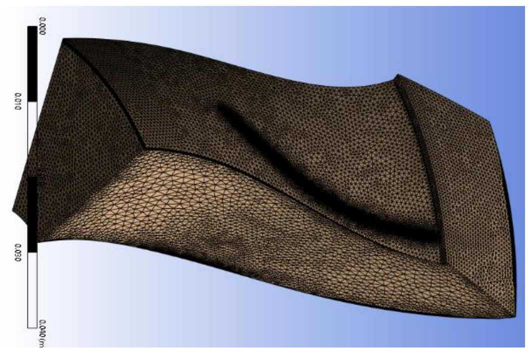

Figure 39 b. Close-up of the wheel's mesh (Shroud side)

Every region as described in Chapter 3.8 was treated accordingly. It is clear in Figures 39a and 39b, that mesh is finer at the blade top and around the blade edges to accurately calculate how the fluid reacts when in contact with the wheel.

Table 7 Wheel Mesh

Object Name	*INLET-SHROUD-BLADE-HUB-OUTLET*	*BLADE TOP*	*SIDE 1 AND 2*	*SHROUD SIDE*
Type				
Element Size Factor		CONFIDENTIAL		
Defeature Size Factor				
Global Size Factor				

Curvature, again, was captured for the wheel shroud and blade with Min Size Factor of [redacted], and [redacted] for the hub.

Outlet

Table 8 Outlet Mesh

Object Name	*INLET-WHEEL NOSE*	*VALVE*	*WALL*
Type			
Element Size Factor			
Defeature Size Factor		CONFIDENTIAL	
Global Size Factor			
Capture curvature			
Curvature Normal Angle			
Curvature Min Size Factor			

Regarding the Outlet, Figures 40a-c show the cross sections of the regions of interest. Figure 40a shows the boundary layers meshed with prisms around the wall and the valve while body sizing in the freestream was employed to accurately represent the flow regime around the valve. Figure 40b focuses on the wheel nose area, and finally, Figure 40c encompasses the entire diffuser, showing the meshing strategy with finer mesh in the regions specified in Table 8 and a coarser global mesh size extending towards the freestream.

Figure 40 a-c. Different Close-ups of the Outlet Mesh

The target element was tetrahedral elements (Tet4) for the free stream, while prismatic elements (Wed6) were used near the walls, where critical variables experience rapid changes, such as the velocity component due to the no-slip condition. For this reason, the inflation method was used to ensure an accurate boundary layer region. The selection of the SST turbulence model required the target y+ to be around 2 for precise boundary layer predictions and adjustment of the prismatic cell layer parameters was performed iteratively by monitoring these values.

For 2 < y+ < 11, the boundary layer will be a blend between wall functions and low-Re formulations and for higher y+ values, SST is adequate but will not deviate much from the k-ε model. With the First Layer Thickness function, the first layer height was [redacted] m with a growth rate of 1.2 meaning every layer is 20% bigger than the previous. The maximum layers were [redacted] for the wheel Shroud, Hub, Blade, and Blade top and 18 for the outlet wheel nose and valve, and both Outlet and Volute walls. CFX provides an automatic near-wall treatment, so Near-Wall formulations will not be further analyzed.

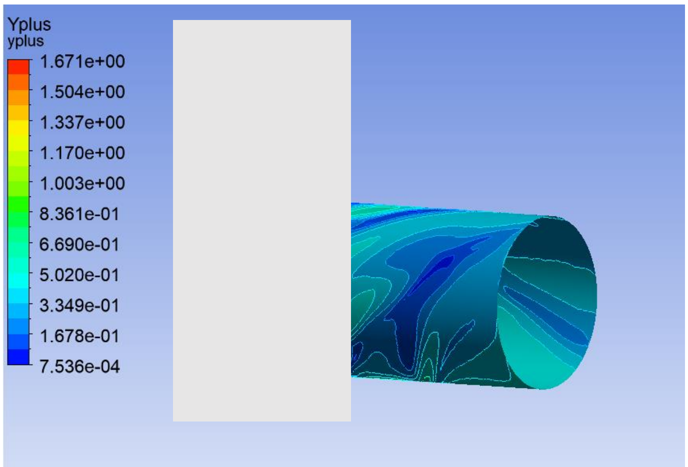

Figure 41 Yplus contour at the diffuser's walls.

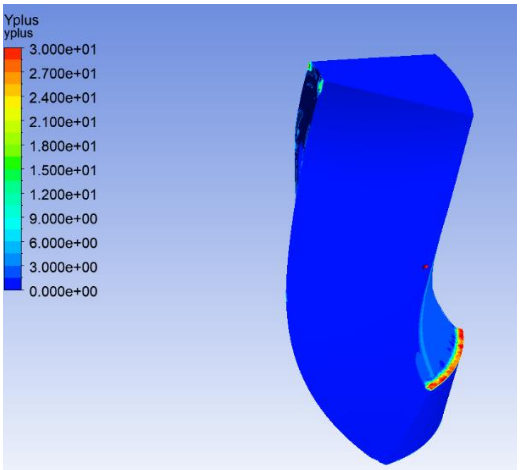

Figure 42 Yplus contour at the wheel.

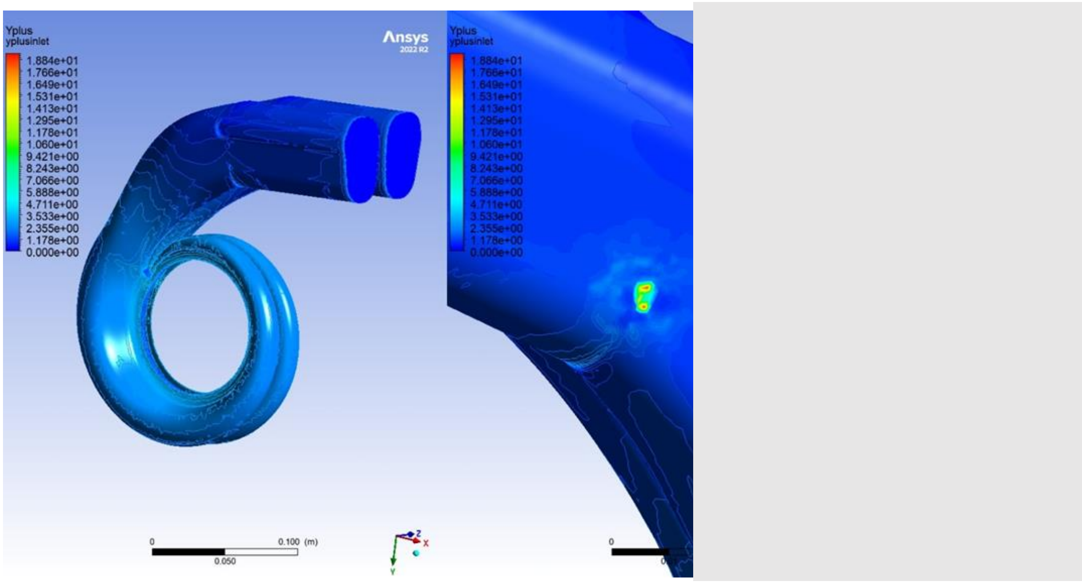

Figure 43 Yplus contour at the volute's wall.

Concerning the y+, it is consistently below 2 in the outlet, as shown in Figure 41. At the wheel [Fig. 42], the y+ is again under 5, with most of the cells reaching the target of 2. Only the shroud area exhibits a peak in the y+ of around 30, which is still considered acceptable considering only a few cells are part of the problematic region. Figure 43 illustrates that the volute wall's y+ target of 2 is reached as recommended, with only a high y+ area present that is automatically treated. Due to its localized nature, this should not introduce any significant discrepancies in the model.

Figure 44 Eddy Viscosity Ratio at the Diffuser's TT plane

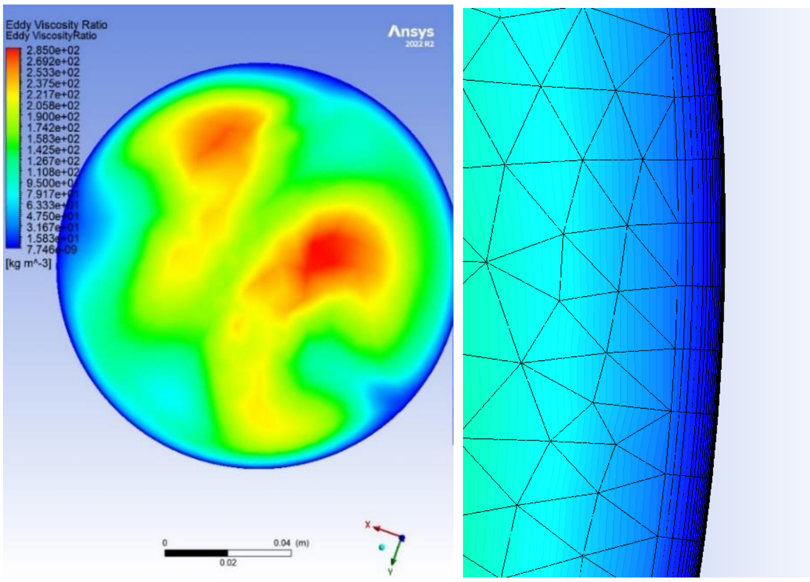

Figure 45 Eddy Viscosity Ratio at the outlet and boundary layer close up

Figures 44 and 45, depict the eddy viscosity ratio for the internal flow based on Eq. 29. The results are realistic as v_R is very low at the boundary layer and increases as turbulence is realized at the main flow.

$$v_R = \frac{v_t}{v}$$

Eq. 29

where v_t is the eddy viscosity and v the dynamic viscosity of the fluid.

4. Turbine Stage Simulation: Case Studies

4.1 Grid Independence Study

A grid independence study was conducted to ensure proper global mesh size with a total of five models tested with elements lengths ranging from 9mm to 5mm. The boundary conditions applied and the target parameters (mass flow and efficiency), are in accordance with the experimental data extracted from the turbine map and can be seen below. In addition to evaluating efficiency and mass flow deviation, secondary parameters such as mesh metrics, the number of elements, and computational time were also considered.

Table 9 B.Cs : Grid Independence

Inlet Total Temperature [°C]	Inlet Total Pressure [Pa]	Turbine Speed (physical) [rpm]	Outlet Static Pressure [Pa]	Measured Efficiency	Measured Mass Flow [kg/s]
[redacted]	[redacted]	[redacted]	[redacted]	[redacted]	[redacted]

4.2.1 Results

Given the complexity of the problem stated and the available resources, a narrower range was selected and analyzed starting with an already fine mesh, to examine more in depth the behavior of the model during element resizing. The simulations were carried out using a cloud service (Rescale), which significantly reduced the time required for computation. In this case, the comparison is qualitative and does not take into account the additional time required for meshing, as this aspect was evaluated locally.

Table 10 Grid Independence Study Results

Model #	Global length [mm]	Number of Elements	Efficiency	Corrected Mass Flow	Timescale
1	9	8185735	[redacted]	[redacted]	-
2	8	9866895	[redacted]	[redacted]	10%
3	7	12247322	[redacted]	[redacted]	21%
4	6	15777793	[redacted]	[redacted]	81%
5	5	21285529	[redacted]	[redacted]	113%

Figure 46 indicates that with a global element size of 0.008 m (Model 2), the efficiency falls within a 0.1% range, and convergence has been achieved. It is important to note that the efficiency deviation contains an error of approximately 5%, which will be discussed further in Chapter 4.2.1 and is used primarily for qualitative convergence depiction.

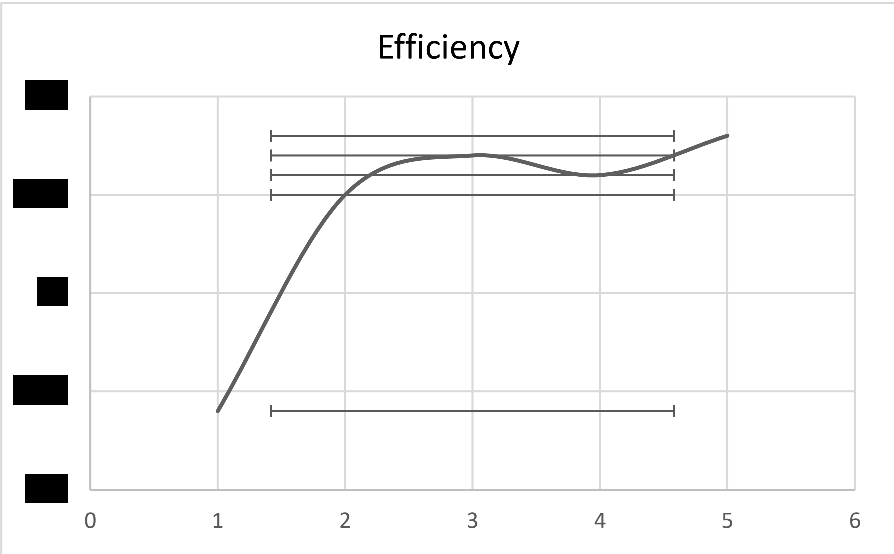

Figure 46 Efficiency Plot for different element sizes

In Figure 47, the corrected mass flow plot is presented and upon closer inspection, although the results are quite similar, Model 3 exhibits a slight drop in mass, which aligns more closely with the test data, followed by an increase after Model 4. Convergence has already been achieved, but this phenomenon may show that a mesh refinement threshold has been reached. Due to the complexity of the model, even slight changes in mesh (~1mm), can impact the flow regime. Coarser mesh [Model 1,2] is not realistic enough and beyond

Model 3, the mesh is too fine, resulting in the solver calculating additional flow features that interfere with the primary flow.

Taking these factors into consideration, along with the significant increase in computational time for each step, the mesh size was decided to be 7mm. Due to the various mesh zones in the model, there is a plethora of parameters to consider, making it a topic for future improvement.

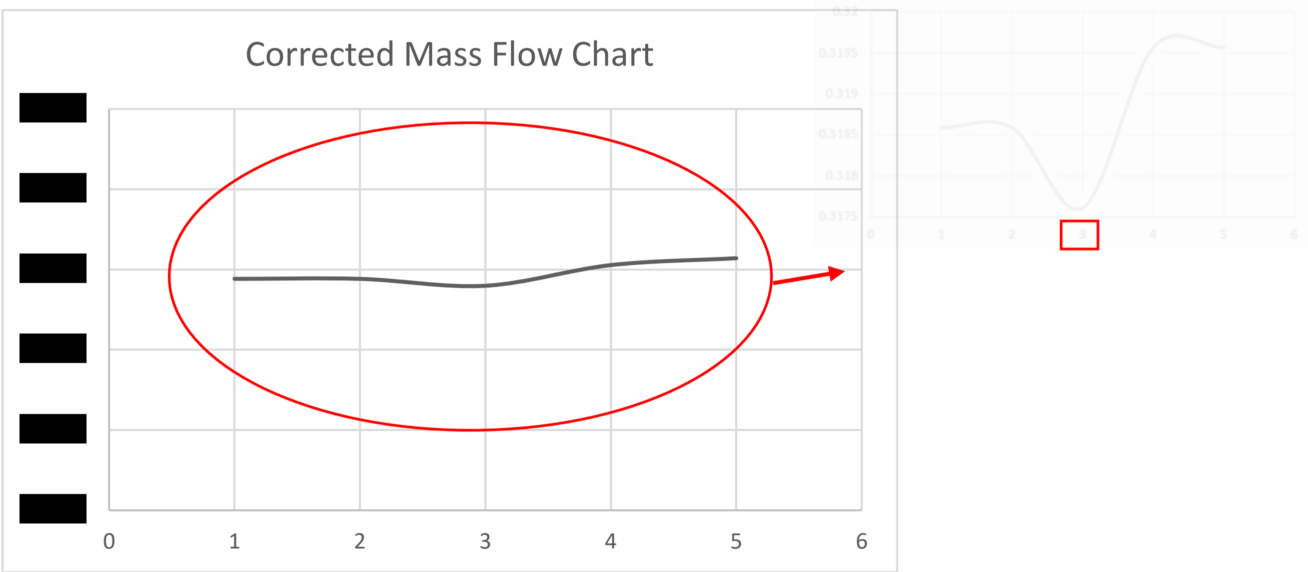

Figure 47 Corrected Mash Flow plot for different element sizes.

4.2 Experimental Evaluation: Gas Stand

A gas stand test was carried out to assess the turbocharger’s performance, reliability, and overall efficiency. This evaluation involved the installation of the turbocharger on the test stand with attention to ensure airtight connections. Furthermore, the test involved mounting the turbine inlet to the manifold and replicating real-world operating conditions.

The performance maps are generated by controlling pressure ratios, engine speed, and mass flow while measuring temperatures and pressures with sensors at both the turbocharger's inlet and outlet. The setup of the Gas Stand Test can be seen in Figure 49. The corresponding turbine map was used to evaluate the model. For this evaluation, twelve design points, listed in Table 10, were strategically selected, with each group represented by a different speed line, starting with a pressure ratio (PR) of approximately 1.4 to decrease uncertainty. Finally, the corresponding turbine map was created by extrapolation.

The input parameters were recalculated by the data [redacted] [Appendix C]. The reference temperature T_{ref} is set to [redacted], P_{1t} was recalculated based on the measured pressure ratios and Turbine speed was set to be the physical speed by multiplying the measured speed as in Eq. 12.

It is important to note that the measured efficiency includes factors such as thermal and bearing losses, geometrical imperfections, and measuring errors. As a result, some deviation between the measured data and simulated data can be expected. This deviation varies depending on the application but is typically within an error margin of 5%. To confidently assess the accuracy of the model, the most crucial parameter to correlate is the measured corrected mass flow, as defined by Eq. 11.

Table 11 BCs: Gas Stand

N,corr [rpm]	Wt,corr [kg/s]	PRT	Efficiency	P1t [Pa]	Nphys [rpm]	DP	Group
[redacted]	[redacted]	[redacted]	[redacted]	[redacted]	[redacted]	1	1
[redacted]	[redacted]	[redacted]	[redacted]	[redacted]	[redacted]	2	
[redacted]	[redacted]	[redacted]	[redacted]	[redacted]	[redacted]	3	
[redacted]	[redacted]	[redacted]	[redacted]	[redacted]	[redacted]	4	2
[redacted]	[redacted]	[redacted]	[redacted]	[redacted]	[redacted]	5	
[redacted]	[redacted]	[redacted]	[redacted]	[redacted]	[redacted]	6	
[redacted]	[redacted]	[redacted]	[redacted]	[redacted]	[redacted]	7	3
[redacted]	[redacted]	[redacted]	[redacted]	[redacted]	[redacted]	8	
[redacted]	[redacted]	[redacted]	[redacted]	[redacted]	[redacted]	9	
[redacted]	[redacted]	[redacted]	[redacted]	[redacted]	[redacted]	10	4
[redacted]	[redacted]	[redacted]	[redacted]	[redacted]	[redacted]	11	
[redacted]	[redacted]	[redacted]	[redacted]	[redacted]	[redacted]	12	

A fully assembled wastegated turbocharger is mounted to the engine to evaluate the efficiency and to produce the maps. Every hole is airtightly closed (see Figure 48), and a stopper is placed at the wastegate to ensure that no mass flow is allowed.

Figure 48 Close up of the assembled turbocharger

Figure 49 Setup of the test and sensors' position.

The extension length was important, as it notes the location of the sensors that are placed at the inlet and outlet measure the corresponding air mass flows, temperatures, pressures, and the turbo speed. In a realistic Gas Stand test, the outlet sensors can be positioned up to one meter away from the turbine outlet. However, in this setup, the distance was approximately 0.5 meters, as indicated by the red boxes in Figure 49. The pipe length, due to the adiabatic wall assumption, can only influence the pressure drop, so two models were tested: Model 1 with the real pipe length [Fig. 50b] and Model 2 with an extension just enough for the flow to be realized as discussed in 3.8.2.

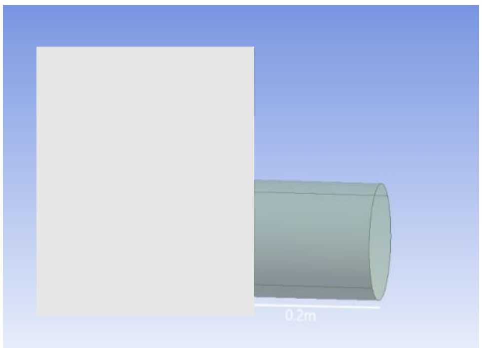

Figure 50 a. Model 2 with overall pipe length of 0.2 m

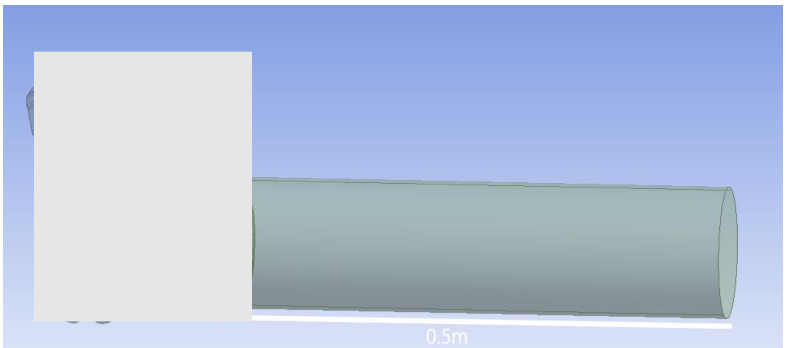

Figure 50b. Model 1 with realistic pipe length

4.2.1 Results

Figure 51 displays the turbine map, with the blue lines representing the map generated by simulations and the red lines representing the corresponding test data measured at specific points. It's worth noting that there is some deviation in the overlap of the efficiency lines, due to insufficient sample for adequate extrapolation. The results of the simulations are shown as light blue and yellow lines in the turbine map, and the data corresponding to these simulations are presented in Table 11. It's evident that both models provide a very accurate estimation of corrected mass flow, with an error that does not exceed 2%.

This demonstrates the effectiveness of the simulation models in predicting corrected mass flow, aligning well with the test data.

Figure 51 Generated Turbine Map with integrated CFX data.

The efficiency lines are shifted up, with a deviation within the 5% margin, which was expected due to the losses mentioned above. The pressure profile varies between the two models, and this can be visualized in Figure 53, which shows the total pressure, along with velocity streamlines. As anticipated, the smaller model (Model 2) exhibits higher outlet pressures because of the shorter pipe length. In Figure 52, the outlet static pressure is presented, and the comparison between the two cases reveals that the difference is relatively small, (~100 Pa). The evaluation was conducted through the whole model without considering only the values at the sensor's locations because it serves only as an estimation and the main focus is how the length affects the overall values extracted by the CFX. The importance of these findings lies, also, in proving that an arbitrary outlet length for the combined turbocharger-catalyst simulation [Chapter 5] can be used as a preliminary approach to understand the system's behavior.

Regarding the gas stand simulation, it serves as a good initial step to validate the setup, but for the purposes of this study, a gas stand test with an open wastegate should be scheduled to gain detailed insights into the behavior of this turbocharger.

Table 12 Gas Stand Test Results

MODEL 1				MODEL 2			
EFF	Wt, corr	%ERR EFF	%ERR Wt	EFF	Wt, corr	%ERR EFF	%ERR Wt
[redacted]	[redacted]	3.66	-0.69	[redacted]	[redacted]	3.39	-0.69
[redacted]	[redacted]	3.93	-0.76	[redacted]	[redacted]	3.40	-0.26
[redacted]	[redacted]	4.36	-1.05	[redacted]	[redacted]	4.36	-1.05
[redacted]	[redacted]	5.29	-0.71	[redacted]	[redacted]	5.01	-0.71
[redacted]	[redacted]	5.51	-0.20	[redacted]	[redacted]	4.86	-0.60
[redacted]	[redacted]	4.46	-0.79	[redacted]	[redacted]	3.67	-1.15
[redacted]	[redacted]	4.40	-1.11	[redacted]	[redacted]	4.66	-1.98
[redacted]	[redacted]	4.55	-0.77	[redacted]	[redacted]	4.55	-1.37
[redacted]	[redacted]	4.65	-0.85	[redacted]	[redacted]	3.48	-1.13
[redacted]	[redacted]	5.38	-1.00	[redacted]	[redacted]	3.07	-1.27
[redacted]	[redacted]	5.37	-0.96	[redacted]	[redacted]	4.11	-1.21
[redacted]	[redacted]	4.90	-0.96	[redacted]	[redacted]	4.38	-1.43

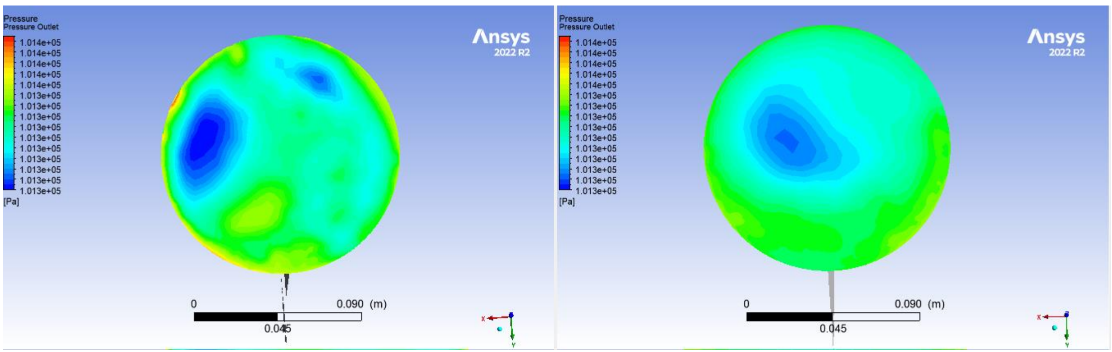

Figure 52 Pressure at the outlet of Model 2 (left) and Model 1 (right)

Figure 53 Total Pressure between Model 2 (left) and Model 1 (right)

4.3 Wastegate Openings Study

Before the description of the turbine with the integrated aftertreatment model, it is essential to first understand the separate behavior of the turbine under changes in the wastegate angle. In total, six models were assessed, with boundary conditions of [redacted] kPa pressure and [redacted] temperature at the inlet, a turbine speed of [redacted] rpm and ambient pressure at the outlet. These boundary conditions were chosen based on testing data and the possibility to correlate them.

Throughout these simulations, the boundary conditions remained constant as the wastegate angle was gradually adjusted. The goal was to observe the efficiency drop and mass flow that occurs as the wastegate angle changes. In a real-world scenario, the wastegate angle depends on the actual operating conditions, and it opens accordingly. In this study, the wastegate angle was controlled via the ECU's signal, as discussed in Chapter 2.4.

The models were evaluated starting from a fully closed valve position (0^{o}) and gradually increasing the angle with a step of 5^{o} until it reaches the fully opened position of 25^{o} for this application. The angle is defined as the angle between the vertical plane, where the poppet is in direct contact with the diffuser wall when full closed and the face of the poppet [Fig. 32 a].

4.3.1 Results

The efficiency experienced a relatively steady loss of around 6% through the first four positions and then the rate declined to 2% and 4% respectively. Likewise, the mass flow through the wastegate increases rapidly to 85% from 0° to 5°, and then the increase flattens to 35%, 15%, and 8% accordingly, as portrayed in Figure 54.

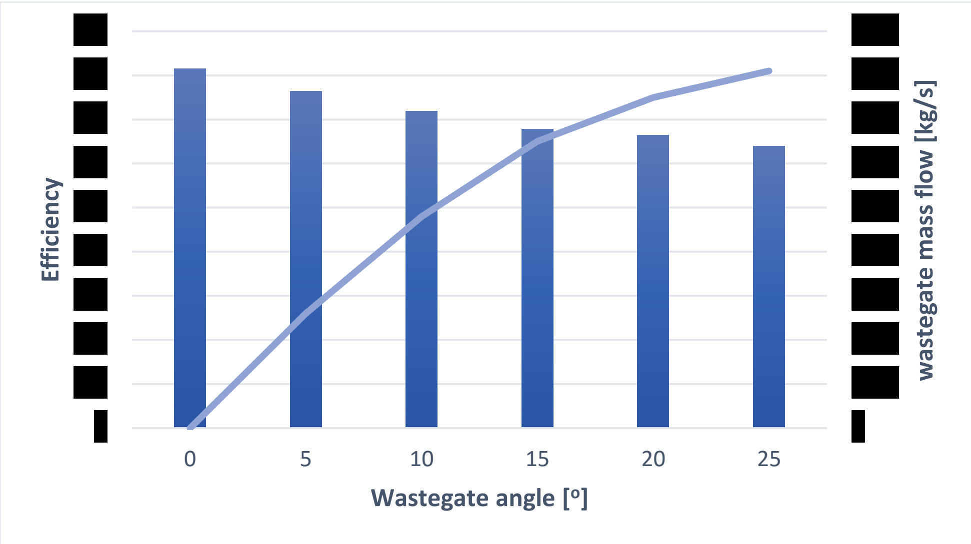

Figure 54 Turbine efficiency and WG mass flow plots for different openings

In Figures 55 a-e, the local pressure distribution at the valve when the air encounters the wastegate is presented. Due to the closed wastegate's modeling approach of placing a wall, the first model has been excluded. The flow patterns are depicted using velocity streamlines that are colored based on the Mach Number (ranging from 0 to 1). The valve is designed to withstand high pressures and it is obvious that pressure minimizes as the channel is opened further. The flow escapes around the valve and hits the walls creating local stagnation points that will prove to be a problem and are studied in detail in Chapter 5.6. This unsteadiness maximizes in the last two models and is more clearly shown in Figures 55 d, e.

Figure 55 Pressure at the Valve and streamlines for different openings.

In Figures 56a-f the velocity contour maps are presented at the TT plane of the diffuser. [redacted] remains attached to the boundary and, due to the Venturi effect, induces [redacted] [redacted] flow diversion away from the central axis. Model 5 [Figure 56e], which represents the 20^{o} opening, exhibits a more stable pattern, largely attributed to the specific angle at which gas impacts the valve and is guided toward the diffuser's neck.

Figure 48 Velocity Contours at the Diffuser for every case (TT plane)

Additional velocity contours at the outlet face of the diffuser are studied [Figure 57 a-f]. The flow loses uniformity progressively with the valve opening, while exiting the diffuser. In these figures, blue areas represent stagnant regions, while at [redacted], there is a maximum velocity zone due to [redacted].

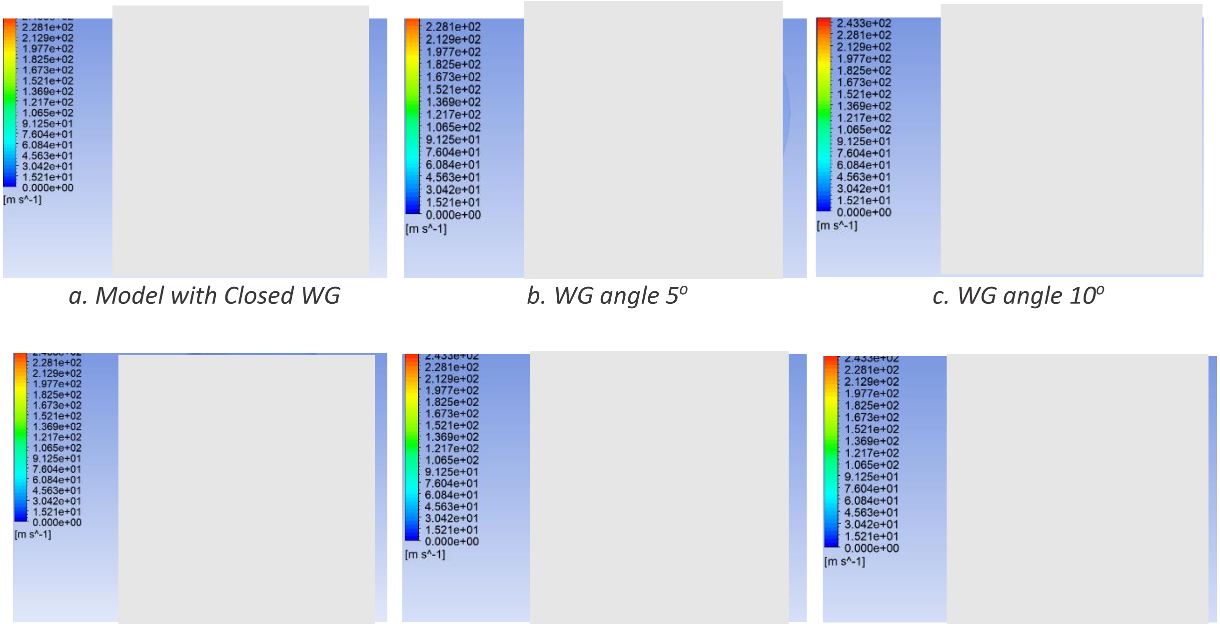

a. Model with Closed WG b. WG angle 5º c. WG angle 10º

d. WG angle 15º e. WG angle 20º f. WG angle 25º

Figure 49 Velocity Contours at the Outlet for every case.

Figures 58 a-f display the temperature distribution at the diffuser outlet. As anticipated, the opening of the wastegate leads to higher temperatures distributed over a larger area. However, due to the geometric constraints of the model, hotspots are generated, while in the majority of the surface, the temperature remains significantly lower.

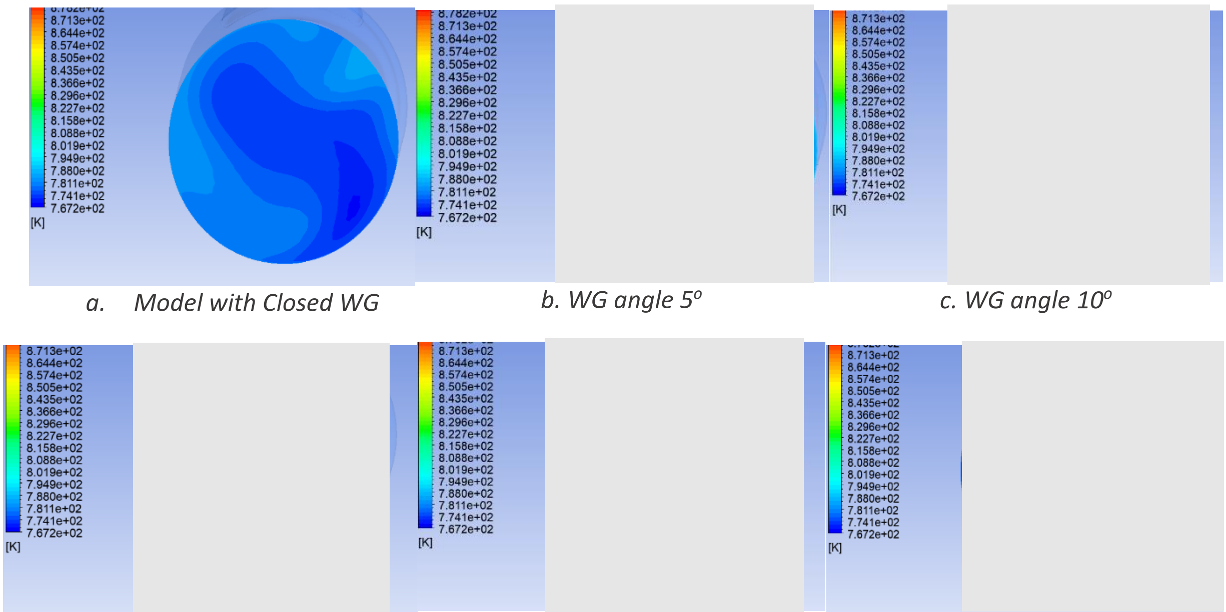

a. Model with Closed WG b. WG angle 5º c. WG angle 10º

d. WG angle 15º e. WG angle 20º f. WG angle 25º

Figure 58 Temperature Contour at the Outlet for every case.

5. Aftertreatment System Design Of Experiment (DOE)

5.1 Introduction

A Selective Catalytic Reduction (SCR) catalyst is one of the preferred methods used to mitigate the environmental impact of internal combustion engines (ICEs), especially diesel engines that produce significantly more NOx emissions. The SCR catalysts are often vanadium or zeolite-based and they are structured in a honeycomb geometry. The function of the catalyst is to turn the harmful NOx into nitrogen (N2) and water with the use of a urea-based agent that is injected into the exhaust steam prior to entering the catalyst. The aftertreatment of a heavy-duty diesel vehicle usually consists also a diesel particulate filter (DPF), a diesel oxidation catalyst (DOC), an exhaust gas recirculation device or other technologies.

Previous studies [24] have highlighted the significance of several parameters in enhancing catalyst performance. Space velocity is an indicator of the residence time inside the catalyst, ultimately affecting the conversion rate. Ageing is also a crucial factor and should be avoided as much as possible for prolonged catalyst life and higher efficiency. The effects of flow distribution at the catalyst inlet, pressure drop, and Light-off time are going to be the focus of this study, and their optimization by utilizing the turbocharger's characteristics are of great importance in the automotive industry.

The software used for the simulation of the catalytic converter was ANSYS CFX. The model consisted of the turbocharger connected to the catalyst through a pipe. Many geometric parameters have been identified as influential factors in the characteristics mentioned earlier and, consequently, in catalytic efficiency. More specifically, the effects of inlet pipe angle [25, 26], pipe length and inlet diameter [27] as well as permeability factors [28,29] have proven to be significant regarding flow distribution and pressure drop.

In this model, the geometry of the catalyst was standard, without parametrization, as a preliminary approach to quantify only the by-pass valve influence. The catalytic converter geometry is based on a standard model, as shown in Figure 59. The pipe length, which affects pressure drop, will remain constant (0.2m) for a qualitative comparison of results. Other common configurations, often characterized by angled or multiple turns due to packaging constraints, along with variable geometric characteristics, could be the focus of future work.

The catalyst comprises a monolith-type substrate and a thin catalytic wash coat, both enclosed in a can. One approach is to individually create multiple representative channels and describe each one in detail before combining them in one macro-model by extrapolation. This approach is a very accurate solution but the representation of the full catalyst [30] is very time-consuming, and one needs to have all the appropriate data for validation. The second, more appropriate in the present case, approach is to simulate the catalyst as a continuous porous medium. Numerous studies [31,33,37] have been conducted regarding this volume averaging method deeming it appropriate and reliable. Despite simplifications at the micro-level, it accurately describes the macro flow behavior, providing a better understanding of the influence of the wastegate angle.

5.2 Setup

The setup consists of the turbine, which was analyzed in the previous chapters, connected to the catalyst as described in the introductory section. The numerical analysis did not account for the chemical behavior of the catalyst, radiation, or buoyancy phenomena. It has been demonstrated that incorporating a non-adiabatic reaction model into a flow model has minimal impact on flow distribution prediction, as indicated by Bennett et al. [32]. Given the significant temperature difference between the exhaust gas and the ambient environment, the walls were assumed to be adiabatic, with thermal conductivity present only in the flow direction.

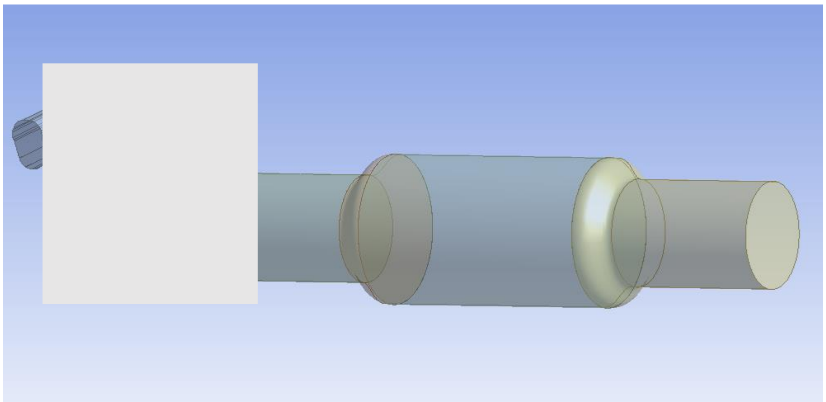

Figure 59 Assembly Visualization in ANSYS

The diffusor or catalyst inlet has a turbulent flow profile that quickly becomes laminar when entering the monolith. Downstream the flow profile is transitional but cannot be captured adequately using the k-ω SST model employed [33], but further examination is beyond the scope of this study.

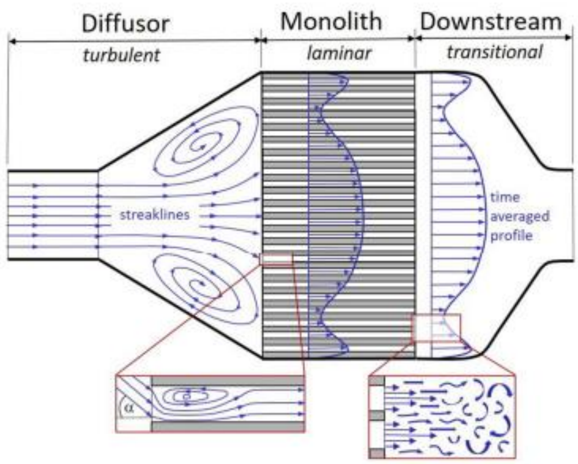

Figure 60 Flow Characteristics inside the catalyst [33]

5.2.1 Flow and Temperature Uniformity

The durability of the catalytic converter and the emission conversion efficiency are greatly impacted by the flow distribution across the catalyst's inlet surface. To quantify the area-weighted uniformity of a variable ϕ, as described in Eq.30.

$$\gamma = 1 - \frac{\sum_{i=1}^{n} [(|\varphi_i - \overline{\varphi_{\text{mean}}}|)A_i]}{2 \cdot |\overline{\varphi_{\text{mean}}}| \cdot A}$$

Eq. 30

The index γ can take values up to 1, targeting as high values as possible for increased uniformity. More specifically, the flow uniformity, first carried out by Weltens et al. [34] will be calculated as:

$$\gamma = 1 - \frac{1}{2}\frac{\sum_{i=1}^{n} |v_i - v_{\text{mean}}|A_i}{Av_{\text{mean}}}$$

Eq. 31

Where v_i describes the local velocity, v_{mean} the average velocity, A_i the local area and A the cross-sectional area of interest. Flow uniformity is key, given that it allows for maximum utilization of catalyst volume.

The corresponding expressions used to calculate the γ index are portrayed in Table 13. For most catalysts, a flow uniformity of minimum 95% should be achieved in order to operate properly so the target γ will be 0.95 and over.

Table 13 ANSYS Code for Flow Uniformity Index

<table>
<tr><td>AV1</td><td>areaAve (Velocity)@ Cat Inlet</td><td rowspan="4">Cat Inlet is a plane created with a slight offset from the catalyst inlet representing the flow regime in the beginning of the monolith.

Measurements were according to the CAD.</td></tr>
<tr><td>Num</td><td>sum (abs (Velocity- AV1) *Area) @Cat Inlet</td></tr>
<tr><td>Den</td><td>2*abs (AV1) *area () @Cat Inlet</td></tr>
<tr><td>Gamma</td><td>1-(Num/Den)</td></tr>
</table>

Another important variable to be quantified is the temperature uniformity where the target is changing depending on the application requirements. High values of γ are not necessarily beneficial if the temperatures are below the light-off and low uniformity depending on where the hotspots are located can be a factor of quicker heat up or cause of ageing.

5.2.2 Pressure Loss

The pressure loss through the aftertreatment is a significant monitor point as it causes excess backpressure, affecting the engine performance. Within the substrate, Reynolds number is below 1000, and therefore, the pressure drop due to the laminarity of the flow is calculated using the modified Darcy's Law with the inclusion of Forchheimer term [Eq. 32].

$$\frac{\Delta P}{L} = -\left(\frac{\mu}{\alpha} v + C_2 \frac{1}{2} \rho v^2\right)$$

Eq. 32

where:

v = superficial flow velocity, which is derived by considering the porosity of the medium [$\frac{m}{s}$]

α = Permeability [m^2]

μ = dynamic viscosity of the fluid [$Pa \cdot s$]

C_2 = Inertial Loss Coefficient [m^{-1}]

L = thickness of porous domain in the flow direction [m]

ρ = fluid density [$\frac{kg}{m^3}$]

For the analytical calculation of the Pressure drop, an excel was created, shown in Appendix D. Figure 75 depicts the deviation between the CFX prediction and the numerical calculation.

The permeability α was set to [redacted] m^2 and C_2 was set to [redacted] $\frac{1}{\mathrm{m}}$ according to the manufacturer data. Based on literature, the transverse loss was described as the streamwise multiplied by coefficients which were set 1000 times greater than actual to ensure there is no lateral flow inside the catalyst. The volume porosity was set to [redacted] and the loss was set to directional with true velocity.

The decision between true and superficial velocity is determined by the placement of the sensors. If during physical testing the sensors are located inside the catalyst, the coefficients are calculated for true velocity. Otherwise, if they are in front of the catalyst, then superficial velocity is used. For this application, the selection was v_{true} due to absence of experimental data.

5.2.3 Velocity Deviation Index

Figures 66a-f depict the velocity profiles at the three planes of the catalyst (inlet, middle, and outlet) where it is evident that high velocities are concentrated in specific spots. Because the variation in magnitude is localized, relying solely on the flow uniformity index is insufficient to provide an accurate description of the flow characteristics. Consequently, an additional parameter, the flow deviation index, needs to be introduced based on:

$$D = \left(\int_{Ai} \frac{|v - v_{mean}|}{v_{mean}} \, dA \right) A_i$$

Eq. 33

The smaller the deviation index, the closest the local velocity magnitude is to the average velocity. Comparable with γ index, they have an inversely proportional relationship aiming for higher flow uniformity values while trying to decrease the deviation as much as possible. A corresponding expression for the D index was programmed, utilizing variables that were described in Table 13. It is important to note that the velocity used in this expression should be specified in the axial direction but, based on the assumption that no lateral flow takes place inside the catalyst, its magnitude equals the overall velocity's magnitude. [18]

5.3 Boundary Conditions

As observed in Chapter 4.3, the temperature profile at the outlet is characterized by hot spot generation. This phenomenon suggests that a fully opened wastegate may not significantly benefit the aftertreatment heat up process if it is not centered, and a redesign of the wastegate channel could be more beneficial. The purpose of this simulation is to quantify the advantages of opening the wastegate at the engine startup for decreasing the heat up time and, thus, increasing after treatment efficiency. For this reason, instead of studying the effect of a fully opened wastegate, six models were assessed [Refer to Chapter 4.3].

A total of two different sets of boundary conditions were applied, as described in Table 14. It was concluded that while using the first set, a wall was placed at the outlet by the solver because of flow instabilities in the first ten iterations. This was in accordance with literature that deems set 2 a more robust set of boundaries for complex applications. Finally, in order for the model to converge without interruptions, the incorporation of an outlet extension was required. The values were derived based on the measurements shown in Appendix B and represent the conditions during the engine's cold start at 900 rpm.

Table 14 BCs: Turbocharger with SCR

SET	Inlet Conditions		Outlet Conditions	Turbo Speed
1	$\boldsymbol{P_{1t}}$=[redacted]	T_{1t} = [redacted]	$P_{2t,stat}$= [redacted] Pa	[redacted] rpm
2	$\dot{\boldsymbol{m}}_{\boldsymbol{t}}$=[redacted] $\frac{kg}{s}$	T_{1t} = [redacted]	$P_{2t,stat}$= [redacted] Pa	[redacted] rpm

5.4 Domains

For the turbocharger domains, please refer to Chapter 3.4. The turbocharger's diffuser section was extended and an interface with the catalyst was integrated in place of the outlet. The additional domains are detailed in Tables 14-16. The catalyst's inlet and outlet regions, highlighted in orange and yellow in Figure 59, were modeled as fluid regions with the same characteristics as mentioned earlier.

Table 15 Catalyst Inlet Domain

Domain	Boundary surface	Boundary type	Details
CAT_IN	Catalyst Inlet Wall	Wall	Smooth, No slip Wall, Adiabatic
	Interface Catalyst Inlet – Diffuser Outlet	Interface	Conservative Interface flux for Mass and Momentum, Turbulence and Heat Transfer
	Interface Monolith-Catalyst Inlet [Side 1]	Interface	Conservative Interface flux for Mass and Momentum, Turbulence and Heat Transfer

Table 16 Monolith Domain

Domain	Boundary surface	Boundary type	Details
CAT_MAIN	Monolith Wall	Wall	Smooth, No slip Wall, Adiabatic
	Interface Monolith-Catalyst Outlet [Side 1]	Interface	Conservative Interface flux for Mass and Momentum, Turbulence and Heat Transfer

	Interface Monolith-Catalyst Inlet [Side 2]	Interface	Conservative Interface flux for Mass and Momentum, Turbulence and Heat Transfer

Table 17 Catalyst Outlet Domain

Domain	Boundary surface	Boundary type	Details
CAT_OUT	Catalyst Outlet Wall	Wall	Smooth, No slip Wall, Adiabatic
	Catalyst Outlet (Exhaust)	Outlet	Subsonic Flow, Mass and Momentum: Static Pressure*
	Interface Monolith-Catalyst Outlet [Side 2]	Interface	Conservative Interface flux for Mass and Momentum, Turbulence and Heat Transfer

The interfaces between the catalyst's inlet, the catalyst and the catalyst's outlet were Fluid-Porous interfaces with a GGI connection while the interface between the diffuser and the catalyst's inlet was defined as Fluid-Fluid.

7.5 Meshing

The meshing for the turbocharger was conducted as outlined in Chapter 3.9. In the case of the catalyst's inlet and outlet, an inflation approach was applied, consistent with the mesh strategy used for the outlet wall. The mesh for the monolith was generated using a sweep method, incorporating a combination of quadrilateral (quad) and triangular (tria) elements. After some initial trial and error, the number of divisions was set to 100. The quality criteria for mesh elements were maintained, resulting in a total element count of 14210769.

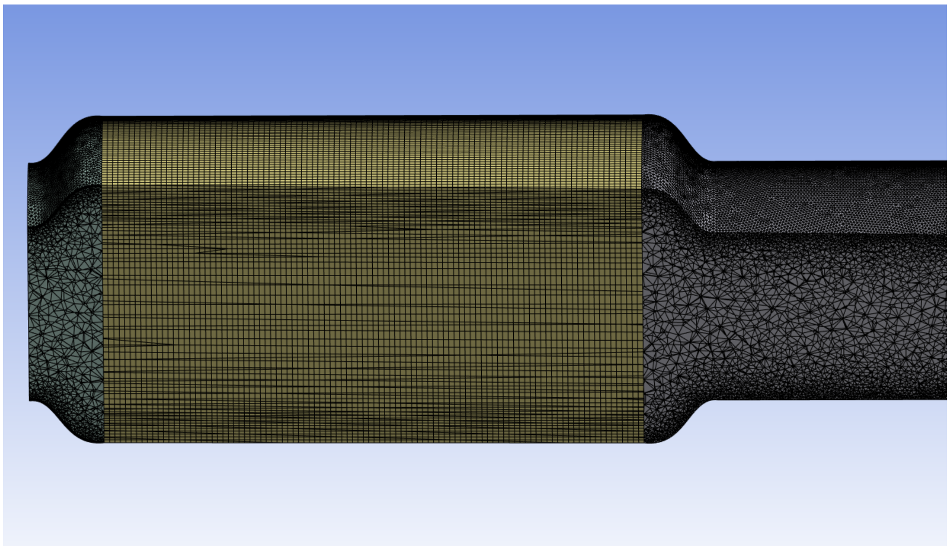

Figure 61 Catalyst Meshing Close up: Sweep Mesh Approach

5.6 Results

Figure 62 provides a side view of the model, showcasing the velocity streamlines that are color-coded to represent fluctuations in Mach numbers. The basic flow characteristics have been captured accurately, as the exhaust gases enter the volute and spin the impeller losing kinetic energy, the Mach number drops from one end to the other. Upon entering the catalyst, the flow exhibits turbulence, but it becomes laminar inside the monolith before transitioning, as illustrated in Figure 60.

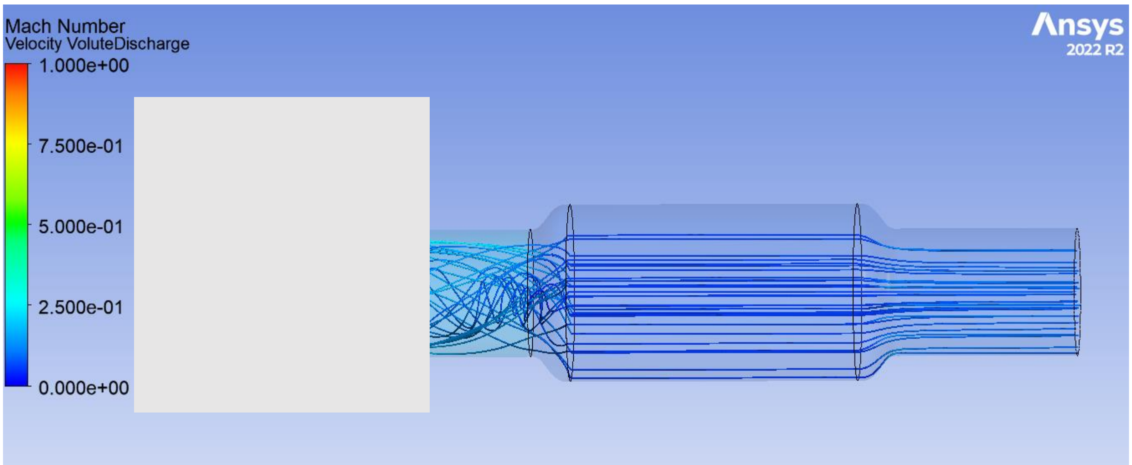

Figure 50 3D velocity streamlines through the whole assembly

Temperature

The temperature contours are displayed in three main planes along the catalyst's length. Moving from right to left, the planes represent the entrance into the substrate, a middle point, and the outlet. In Figures 63 a-f, the contours depict the local temperature calculated in every model for easier comparison. The temperature exhibits a noticeable increase in the first four valve opening positions, but locally drops in the fully open position, and the hot spot is not clearly evident. This phenomenon will be further explained in the following sections.

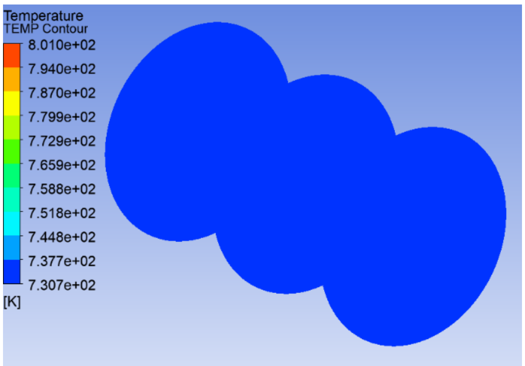

a. Model with Closed WG

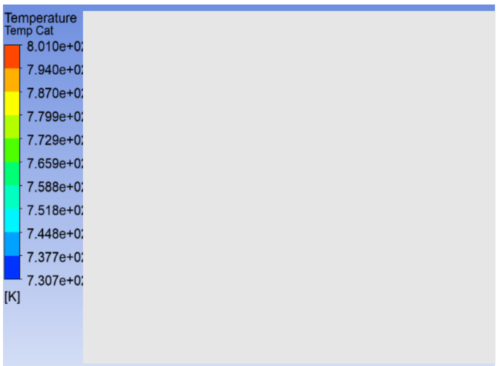

b. WG angle 5°

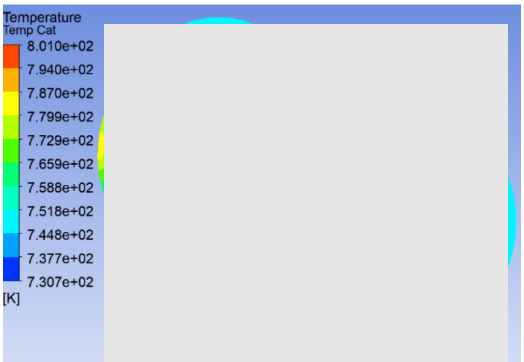

c. WG angle 10°

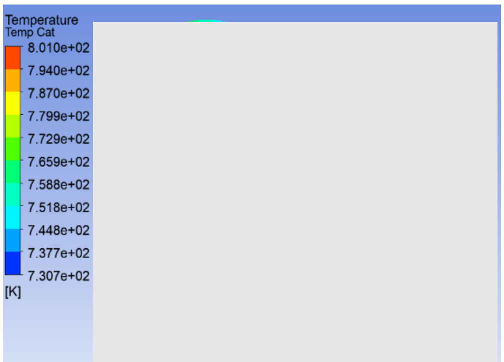

d. WG angle 15°

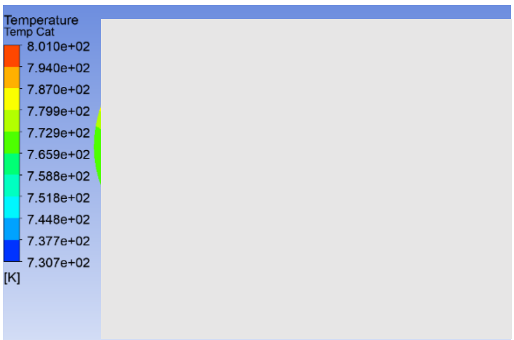

e. WG angle 20°

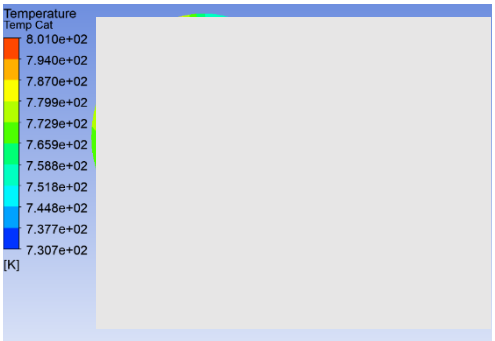

f. WG angle 25°

Figure 51 Local Temperature Contours at the catalyst's main planes for all domains.

Despite the hot spot generation, there is a gradual trend toward temperature homogenization, which is more clearly depicted in Figures 64 a-f, where the contours are plotted in regards with the individual model's temperature variations. Although a closed wastegate provides a more uniform profile, the maximum value is 65° C lower than the one achieved with a wastegate opening of 20°.

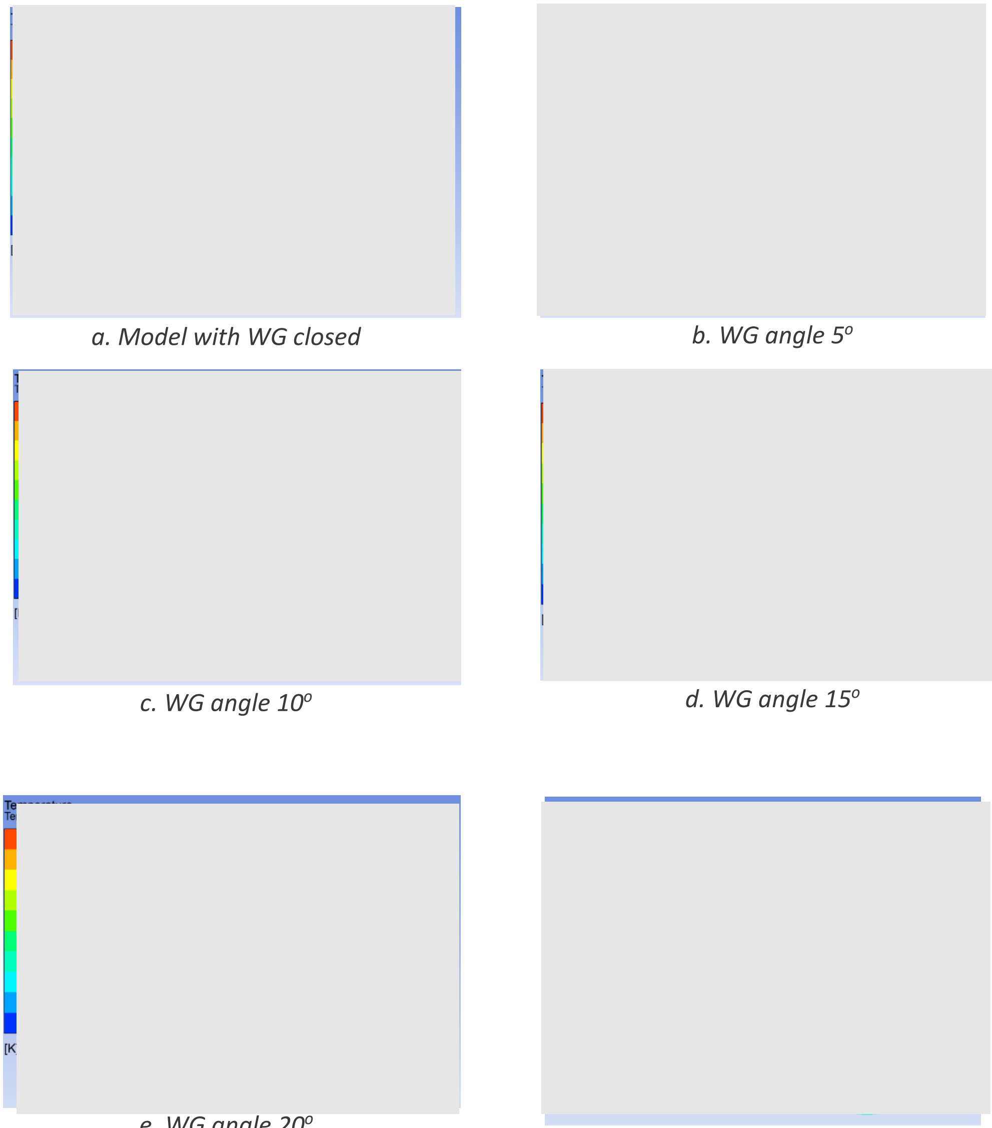

a. Model with WG closed

b. WG angle 5°

c. WG angle 10°

d. WG angle 15°

e. WG angle 20°

f. WG angle 25°

Figure 64 Local Temperature Contours at the catalyst's main planes for individual domains

Generally, hotspots should be avoided because increased temperature in a targeted region can cause operational problems like local yielding, which deteriorates the quality of the aftertreatment device. During cold start, the variations are not large enough for the locality to become a problem but should be taken into consideration for higher engine speeds and may require further studying. Finally, depending on the application and the SCR's requirements, a middle range opening can be beneficial due to the trade-off between hot-spot generation and uniformity.

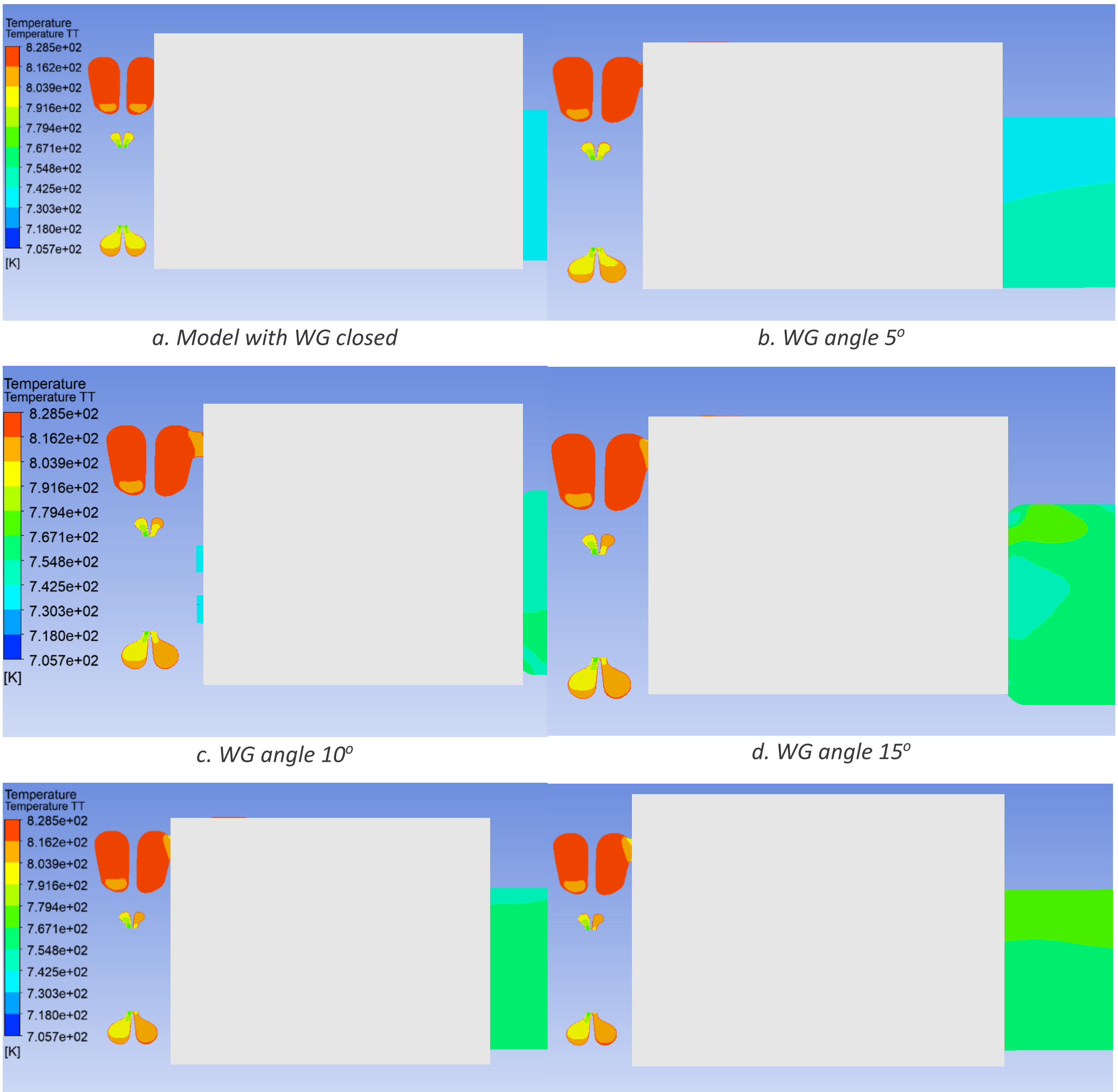

a. Model with WG closed | *b. WG angle 5°*

c. WG angle 10° | *d. WG angle 15°*

e. WG angle 20° | *f. WG angle 25°*

Figure 65 Temperature Contour at The TT Plane for different cases.

Figures 65 a-f, show the effects of the detachment of the flow in the temperature field. It is important to note that high temperatures near the walls indicate that a non-adiabatic study would be beneficial to have a better understanding of the dynamics during cold start and how they influence the results.

Velocity

As demonstrated previously, the gases decelerate as they enter the substrate due to the porosity and regain some of their kinetic energy at the outlet region. As discussed, flow uniformity is crucial in to take advantage of the whole catalyst's volume. Regarding Figures 66 a-f, the velocity contours inside the catalyst are shown, and it is visible that the gradient change rapidly [redacted] due to the wastegate's channel positioning. It is clear that the middle section depicts the lowest entrance velocity as recirculation occurs.

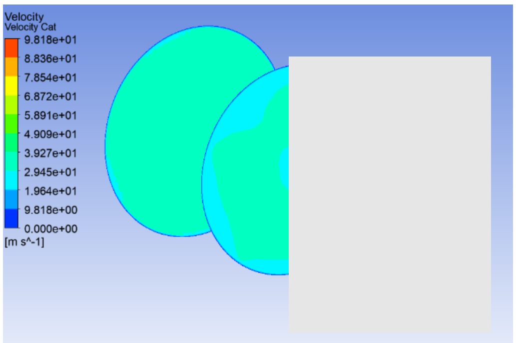

a. Model with WG closed

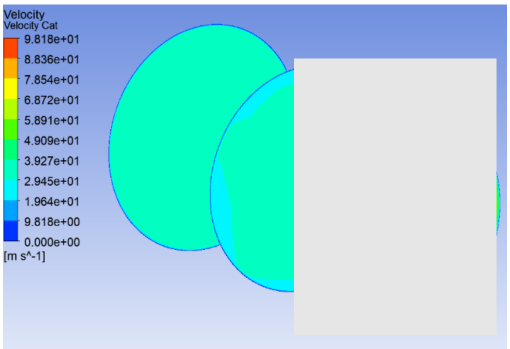

b. WG angle 5°

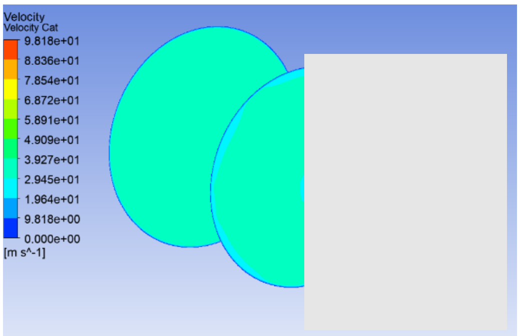

c. WG angle 10°

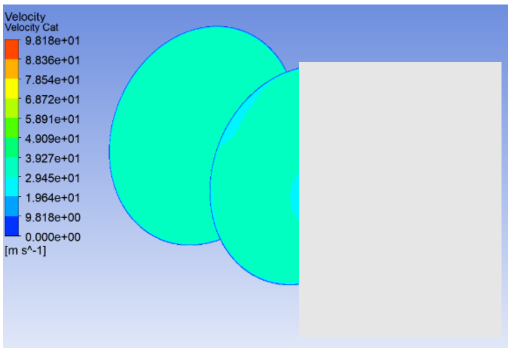

d. WG angle 15°

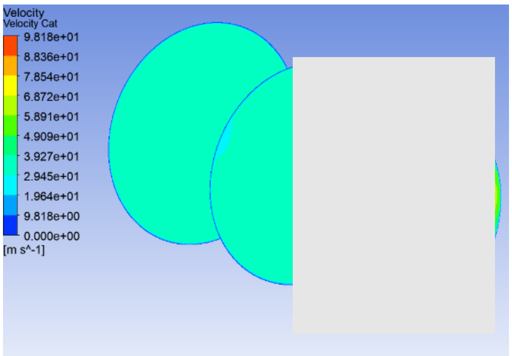

e. WG angle 20°

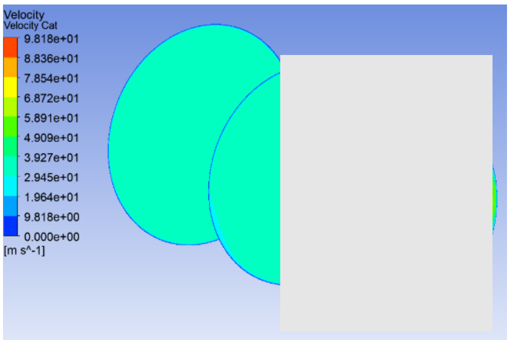

f. WG angle 25°

Figure 66 Local Velocity Contours at the catalyst's main planes for all domains

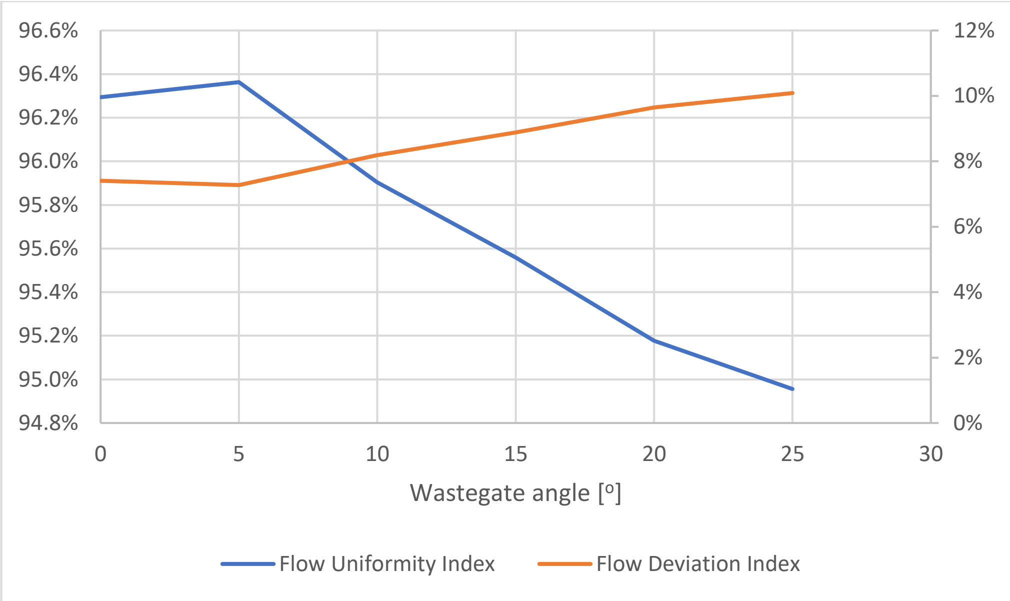

Figure 67 γ Index vs D Index plot at various openings

As previously explained, the flow uniformity index alone is not very representative in this case, so Figure 67 shows the plot of γ vs the velocity deviation. As the wastegate opens further than 10º, both factors deteriorate rapidly, with the best combination seeming to be the 5º opening. In the fully opened position, the 95% target is not reached, but it remains within acceptable limits.

Figure 68 offers a closer look into the velocity vector in the Middle Plane (TT) of the fully open model, providing insights into the flow characteristics and how the fundamental features of this system impact the overall process.

In Figure 69, it is evident that the angled valve divides the flow as a portion of the gas escapes over the top of the valve into the wastegate channel, creating vortices. This is not necessarily a bad thing, as it redirects the separated flow back into the main channel at the neck. However, the channel design does not allow the wastegate flow to enters smoothly the main flow, as it hits the wall creating a major stagnation point and ultimately, reattaching fully in [redacted], forming a [redacted].

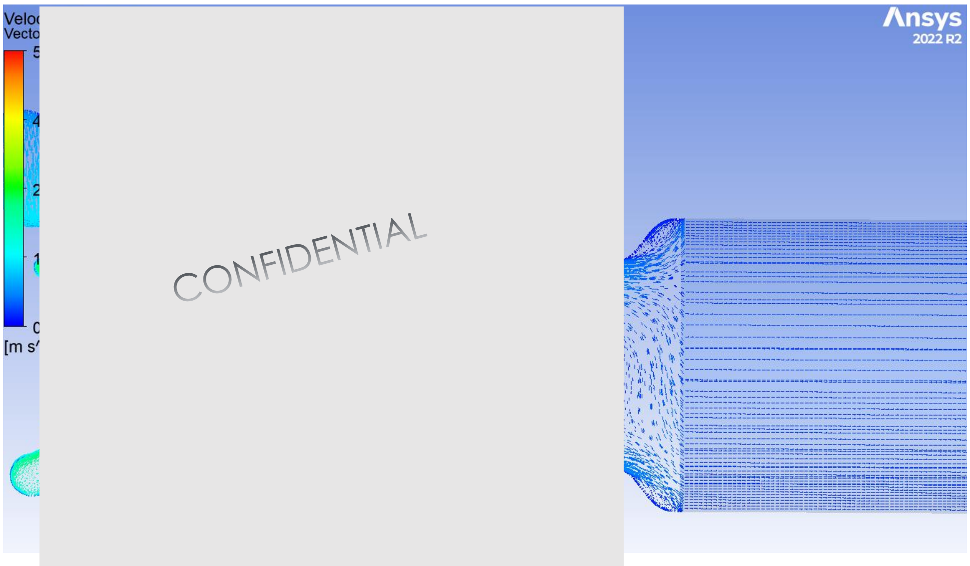

Figure 68 Velocity Vectors at the TT Plane of the assembly

Figure 69 Close Up on the velocity vectors at the valve Channel

Looking at Figure 70, it is obvious that wastegate flow amplifies the flow at [redacted], while a less prominent profile is observed at [redacted]. There are three main vorticities in the main channel, two of which can be attributed to low turbine speed and are to be expected, as they are in front of the turbine wheel. The third vorticity on the right side, is due to the fluid recirculation caused by the high porosity of the catalyst. By extending the inlet of the catalyst, the latter vorticity can be contained in the front face of the substrate, which generally benefits the catalytic process, while also limiting its interference with the main flow in order to keep the static pressure contained.

Furthermore, there is a noticeable boundary layer separation on both sides of the aftertreatment's inlet. When combined with the higher velocity on the [redacted], this phenomenon generates another vorticity at the top corner. This vorticity should be avoided as it can lead to soot concentration and negatively impact the efficiency of the system.

Figure 70 Close up on the velocity vectors at the main channel

Pressure

It can be observed in Figure 71, that an important pressure drop occurs within the porous region due to the inertial and viscous resistance of the porous media. The biggest pressure loss is in the middle section, where the fluid velocity changes as it passes through the catalyst.

In a similar manner, the Pressure is presented in terms of Local Pressure range through all the cases at the inlet [Figs.72 a-f] and middle section [Figs. 73 a-f]. The outlet contours were omitted, as they have a consistent pressure profile decreasing gradually at the middle section.

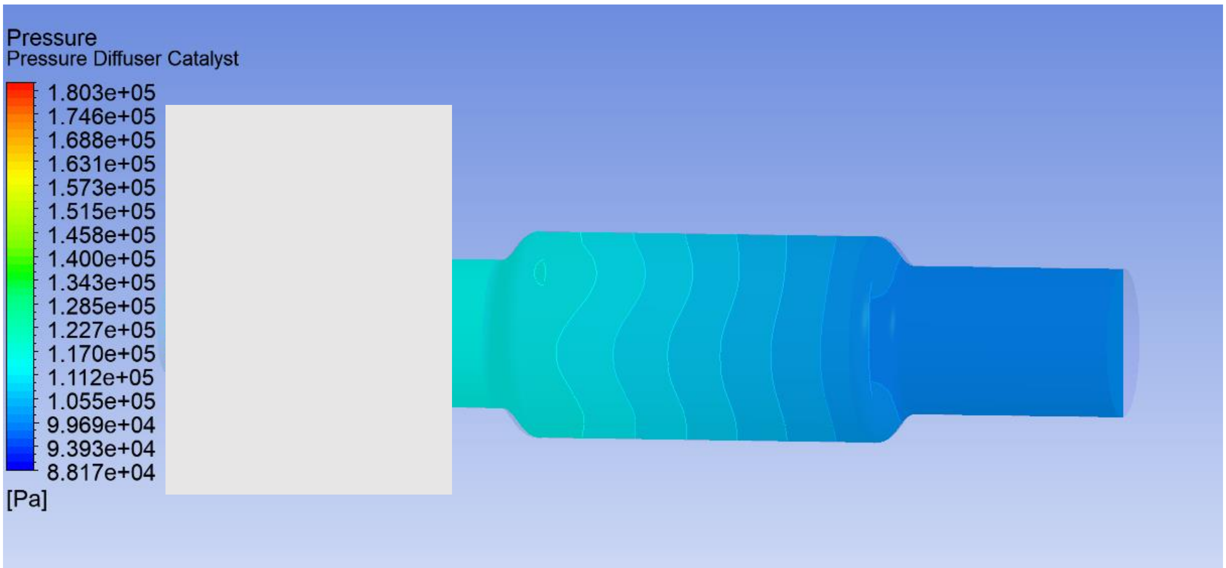

Figure 71 Pressure Contour through the TT section of the whole assembly

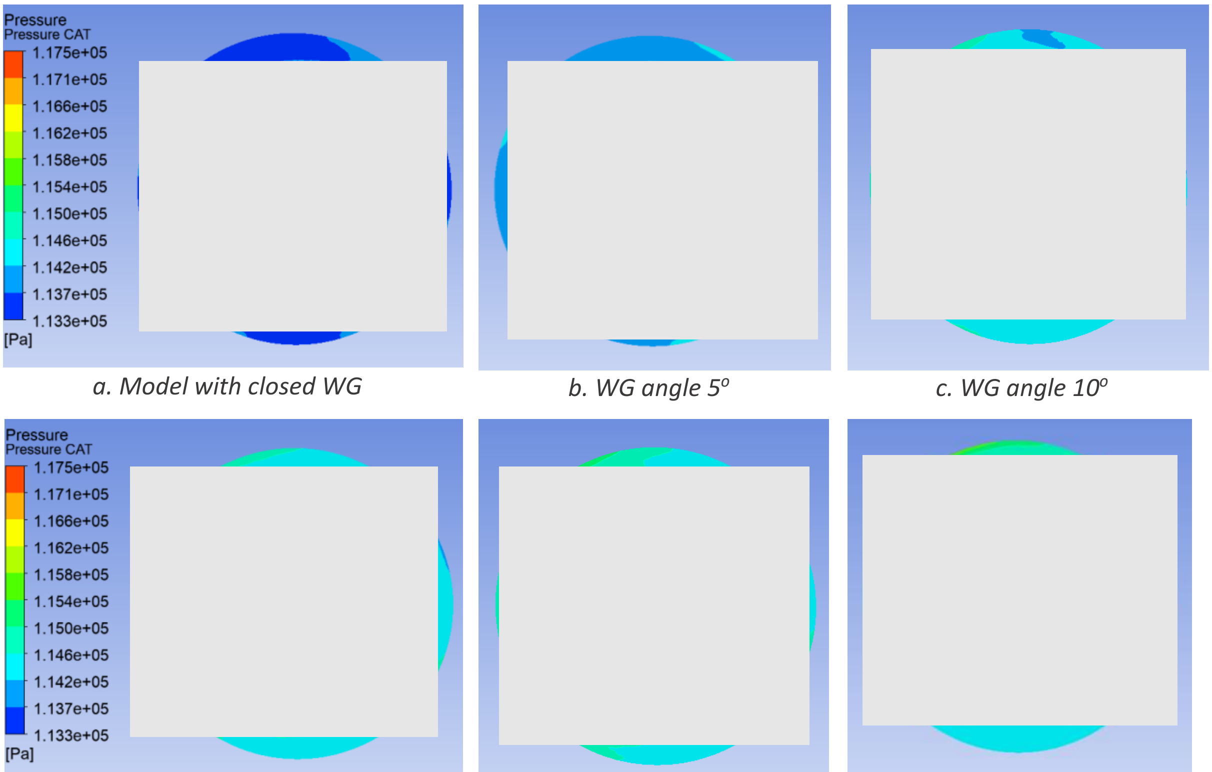

a. Model with closed WG *b. WG angle 5°* *c. WG angle 10°*

d. WG angle 15° *e. WG angle 20°* *f. WG angle 25°*

Figure 72 Pressure Profiles at the Inlet plane of the catalyst

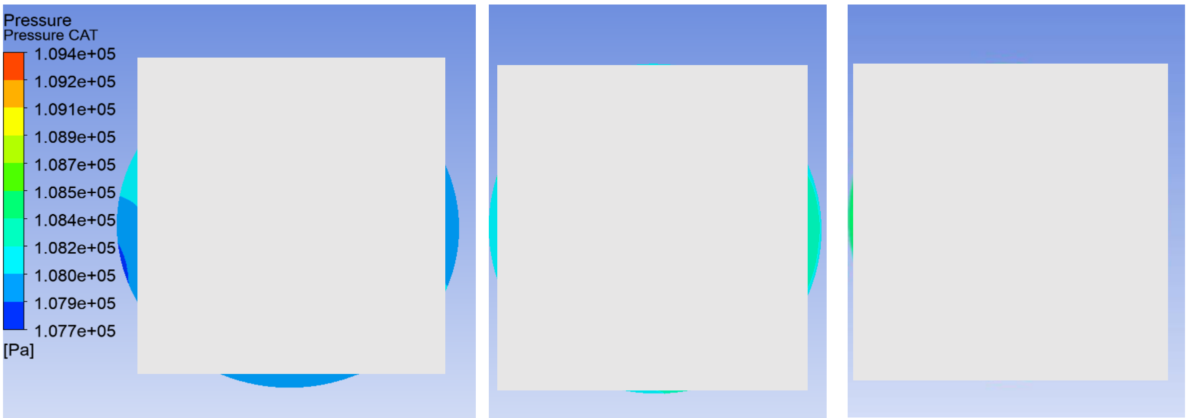

a. Model with closed WG *b. WG angle 5º* *c. WG angle 10º*

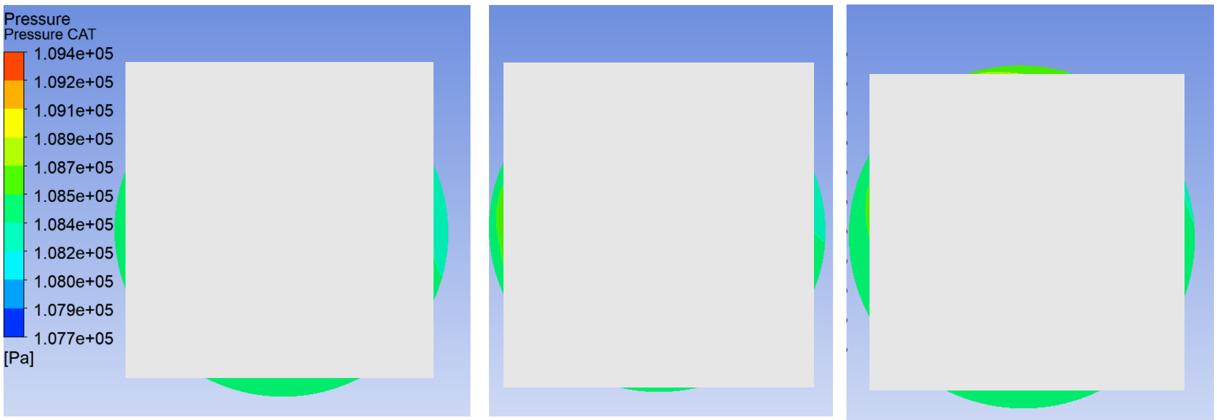

d. WG angle 15º *e. WG angle 20º* *f. WG angle 25º*

Figure 73 Pressure Profiles at the middle plane of the catalyst

The pressure drop was calculated inside the monolith as the difference of the average values in the planes II-II, portrayed in Figure 74. The total pressure drop through the whole device was quantified in the same manner at the planes I-I.

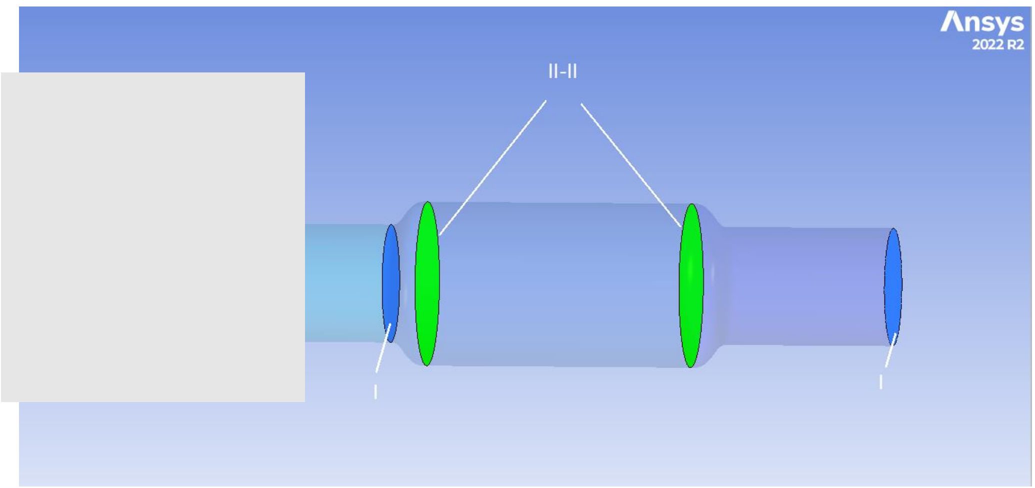

Figure 74 Planes I-I, and II-II that represent the different measurement points.

The values were also calculated analytically, by utilizing the excel [Appendix D] based on Eq. 30. Figure 75 presents a comparison between the simulation-derived values and the calculations, deeming the simulation a relatively accurate representation with an error of prediction not exceeding 5%.

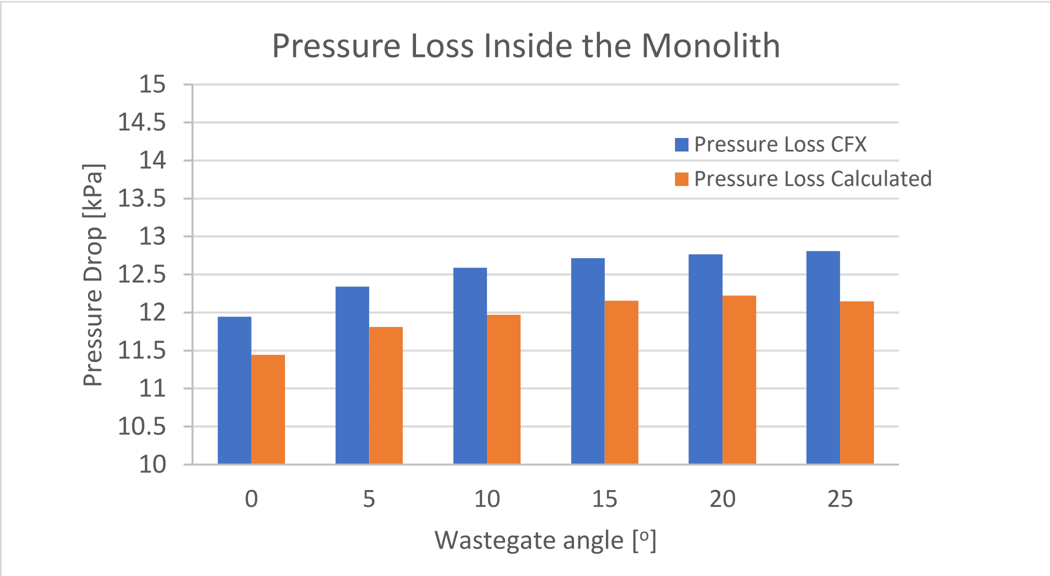

Figure 75 Calculated vs Simulated Monolith Pressure Loss on different angle openings.

Figure 76 depicts the plot of the pressure loss through the whole device for every wastegate angle opening. Data has proven that by opening the wastegate after 10º, the pressure drop remains relatively stable and does not peak. Especially between 15º-20º, it is almost identical, portraying a difference of only 7 Pa.

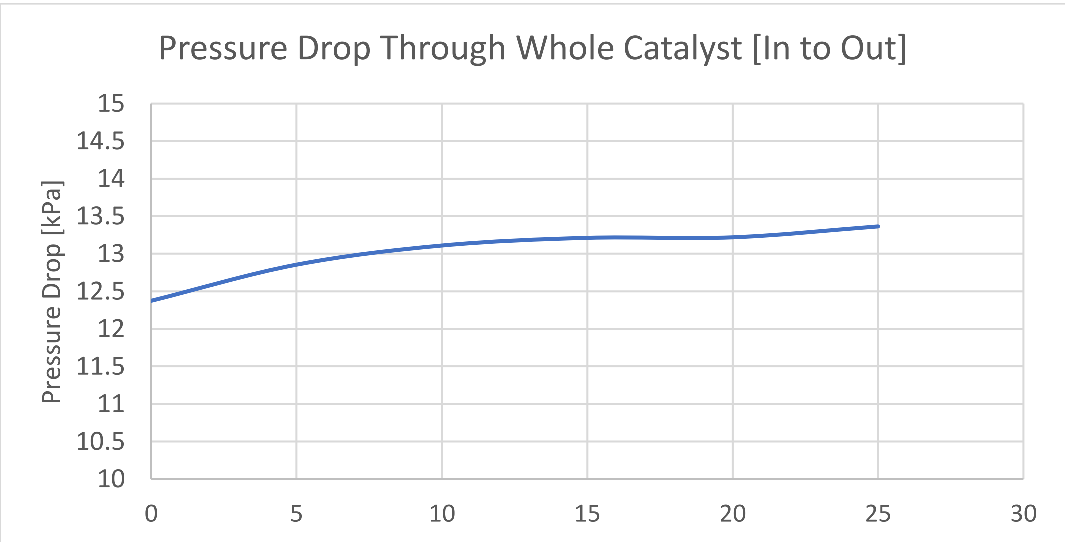

Figure 76 Pressure Loss trend through Catalyst at different angles.

6. Conclusions and Recommendations

6.1 Conclusion

This Diploma thesis focused on investigating the impact of the wastegate valve's opening angle on the warm-up process of a specific commercial vehicle's turbocharger to the catalyst during cold start. The study involved the development of a reliable turbine-side model for the turbocharger, which was extensively described and validated against real measurements obtained from a Gas Stand. For the turbocharger model, the extensions with a minimum of [redacted] diameter were proved to be satisfactory, and the results converged effectively. The meshing target length was also examined and for the particular application, further refinement was deemed unnecessary. The opening angle effects were simulated separately at first, before introducing the catalyst model, to better visualize the stand-alone behavior.

Regarding the Selective Catalytic Reactor, different approaches were evaluated for the setup, with the sweep meshing combined with the porous media approach and the specific set of boundaries, as described, proving to be the most suitable. The boundary conditions were based on the engine specifications and were kept constant throughout the simulations to assess the impact of the different openings.

While there are numerous unexplored parameters, which will be listed in the next subchapter as recommendations, the study concluded that a fully opened wastegate is not recommended. Considering the flow reintroduction angle, an opening between 15^o-20^o is more desirable, for the smoother main flow realization. Pressure Losses after 10^o remain relatively stable, and a peak of Temperature happens at the 20^o opening. Additionally, the drop in the efficiency of the turbocharger flattens after 15^o with a relative drop of less than 2% at the 20^o mark. Uniformity and deviation of the velocity quickly deteriorate after 10^o but γ drops below 95% only at the fully open position.

6.2 Recommendations

Throughout this research, adiabatic wall conditions were assumed. To fully understand how the through-wall heat transfer affects the results, a fully diabatic model should be assessed, considering all the losses that may occur [35]. Furthermore, there is room for improvement by conducting a transient analysis of the system. This would involve incorporating the engine's pulses by feeding the inlets at separate times to capture all the specific characteristics related to twin-scroll setups. Finally, the next step for the validation involves the scheduling of Gas Stand test with variable waste gate openings.

In terms of system design, the model represented a basic configuration, and it is possible to be improved. One approach is to decrease the catalyst inlet angles to prevent the local vorticity and, in the absence of soot concentration, the catalyst efficiency will increase. Other geometries should be evaluated as well as changes in the inlet diameter, the pipe angle, or the pipe length, which are key factors of the overall behavior during cold start. This redesign can be a future step and the model can be tested with thermocouples at the catalyst to validate the simulation.

Some suggestions are the redesign of [redacted], increasing the uniformity and minimizing the thermal losses that may occur while it is mostly boundary-bend. A similar study was conducted for a simple PV turbocharger and has shown that the angle of reintroduction significantly increased the efficiency of the catalyst [36]. The diameter of the valve can also be increased to prevent the gas from flowing over it in most configurations [46], although it should be studied how it will be affected by the local pressure.

7. Appendix

Appendix A: [redacted] Test Results

Appendix B: Engine Data Excel

CONFIDENTIAL

Appendix C: Gas Stand Data Excel

CONFIDENTIAL

Appendix D: Pressure Drop Calculation Excel

Density

$$\rho = \frac{P_{2,stat}}{r.T_{2,stat}}$$

$$v = \frac{Q}{S\,\rho}$$

p cat	113921	Pa
r	361	J/kg/K
T cat	734	K
Density	**0.4297**	**kg/m³**

Area	0.024964	m²
Mass flow	0.300228	kg/s
Density	0.4297	kg/m³
v channel	28.0	m/s

porosity	0.8072	-
v porous	**34.7**	**m/s**

Permeabili	2.46E-08	m^2
Intertial Lo	4.67	1/m

Dynamic V	3.37E-05	kg/m/s
Velocity	28.0	m/s
Length	0.290145	m

Pressure d	**11342.97**	Pa

8. References

[1] S.L Dixon and C.A Hall (2013) *Fluid Mechanics and Thermodynamics of Turbomachinery* ,7th ed. Butterworth-Heinemann , ISBN: 0123914108, 9780123914101

[2] Garrett Motion Inc (2019) *Turbo Tech 101 - Basic: Understanding the Parts of the Turbocharger,* https://www.garrettmotion.com/knowledge-center-category/oem/basic/

[3] Garrett Motion Inc (2019) *Turbo Tech 103 - Expert: Compressor Mapping,* https://www.garrettmotion.com/knowledge-center-category/oem/expert/

[4] Hung Nguye-Schafer (2015) *Rotordynamics of Automotive Turbochargers* ,Garrett Advancing Motion, Internal Trainings

[5] Steven Zhu *Turbocharger Materials* ,Garrett Advancing Motion, Internal Trainings

[6]N. C. Baines (2005) *Fundamentals of Turbocharging,* Concepts NREC , ISBN: 0933283148, 9780933283145

[7] Garrett Motion Inc (2023) *Turbo Tech: Turbine Housings 101,* https://www.garrettmotion.com/news/newsroom/article/turbo-tech-turbine-housings-101-garrett-performance/

[8] George Keith Batchelor (1967) *An Introduction to Fluid Dynamics ,* Cambridge University Press, ISBN: 0521663962, 9780521663960

[9] H. K Versteeg and W. Malalasekera (2007) *An Introduction to Computational Fluid Dynamics: The Finite Volume Method*, 2nd ed. Pearson Education Limited, ISBN: 978-0-13-127498-3

[10] J.O Hinge (1975) *Turbulence*, McGraw-Hill Publishing Co., ISBN: 0070290377, 9780070290372

[11] A. Dimelow (2018) *Steady and transient conjugate heat transfer analysis of a turbocharger,* 13th International Conference on Turbochargers and Turbocharging, Institution of Mechanical Engineers (IMechE), ISBN: 978-1-5108-7387-2

[12] Gibson, L., Galloway, L., Kim, S., and Spence, S. (2017) *Assessment of Turbulence Model Predictions for a Centrifugal Compressor Simulation*, Journal of the Global Power and Propulsion Society.

[13] F. R. Menter, M. Kuntz, and R. Langtry (2003) *Ten Years of Experience with the SST Turbulence Model*, Turbulence, K. Hanjalić, Y. Nagano and M. Tummers (editors) Heat and Mass Transfer 4, pages 625-632, Begell House Inc.

[14] F. R. Menter (1994*) Two-Equation Eddy-Viscosity Turbulence Models for Engineering Applications*, AIAA Journal Volume 32 No. 8 pages:1598-1605

[15] A. Romagnoli, A. Manivannan, S. Rajoo, M.S. Chiong, A. Feneley, A. Pesiridis, R.F. Martinez-Botas (2017) *A Review of Heat Transfer in Turbochargers*, Renewable and Sustainable Energy, DOI: 10.1016/j.rser.2017.04.119

[16] S. Alaviyoun, M. Ziabasharhagh and A. Mohammadi (2022) *A Three-Dimensional Conjugate Heat Transfer Model of a Turbocharger Turbine Housing,* Iranian Journal of Science and Technology, Transactions of Mechanical Engineering Volume 46 pages: 71-84

[17] Martin Babak (2017) *Turbine Design, Operation and Performance*, Garrett Advancing Motion, Internal Trainings

[18] Zhang X, Gomulka T, Romzek M. (2007) *Numerical optimization of flow uniformity inside an F-oval substrate*. SAE technical paper no. 2007-01- 1088.

[19] V. Jyothishkumar, M. Mihaescu, B. Semlitsch, and L. Fuchs (2013) *Numerical flow analysis in a centrifugal compressor near surge condition*. AIAA Paper: AIAA2013-2730

[20] R.C. de Souza, C.C. Krieger Filho (2011) *Automotive Turbocharger Radial turbine CFD and Comparison to Gas Stand Data*. SAE technical paper no. 2011-36- 0081, ISSN: 0148-7191

[21] Shah, S. P., S. A. Channiwala, D. B. Kulshreshtha and G. Chaudhari (2016) *Study of flow patterns in radial and back swept turbine rotor under design and off-design conditions*. Journal of Applied Fluid Mechanics 9(4), 1791-1798.

[22] ANSYS, Inc. (2016) ANSYS Fluent User's Guide, Release 17.2

[23] Dnyanesh Dandekar, Harinivas Bala, Veera Vishnu (2022) *The Impact of Turbo Swirl Effect on Gas Flow Uniformity in Catalytic Converter and Modeling Methodology*, IJSET Vol. 10(8) ISSN(O): 2348-4098

[24] Martin, A., Will, N., Bordet, A., Cornet, P. et al. n (1998) *Effect of Flow Distribution on Emissions Performance of Catalytic Converters*, SAE Technical Paper 980936, ISSN:0148-7191

[25] Thundil Karupparaj R, Ramsai R. *Numerical study of fluid flow and effect of inlet pipe angle in catalytic converter using CFD*, Research Journal of Recent Sciences ISSN: 2006:2277-502

[26] Aniket Patil et al (2019) *A Numerical Study of fluid flow and Pressure Drop analysis of Catalytic Converter using Commercial CFD code* IOP Conf. Ser.: Earth Environ. Sci. 312 012032

[27] Om Ariana Guhan C.P., G. Arthanareeswaran, K.N. Varadarajan, S. Krishnan (2016) *Numerical optimization of flow uniformity inside an under body- oval substrate to improve emissions of IC engines*, Journal of Computational Design and Engineering 3 ,198–214 https://doi.org/10.1016/j.jcde.2016.02.001

[28] Soo-Jin Jeong, Woo-Seung Kim (2003) *A study on the optimal monolith combination for improving flow uniformity and warm-up performance of an auto-catalyst* , Chemical Engineering and Processing: Process Intensification Volume 42, Issue 11, 879-895 https://doi.org/10.1016/S0255-2701(02)00140-X

[29] R.E. Hayes , A. Fadic, J. Mmbaga, A. Najaf (2012) *CFD modelling of the automotive catalytic converter*, Catalysis Today 188 94–105 https://doi.org/10.1016/j.cattod.2012.03.015

[30] J.P. Leclerc, D. Schweich, H.I. de Lasa, et al. (1993) *Chemical Converter Technology for Environmentally Safe Converters and Products*, Kluwer Academic Press, Dordrecht p. 547

[31] Porter, S., Yamin, A., Aleksandrova, S., Benjamin, S., Roberts, C., & Saul, J. (2014) *An Assessment of CFD Applied to Steady Flow in a Planar Diffuser Upstream of an Automotive Catalyst Monolith*. SAE International journal of engines, 7, 1697-1704.

[32] Will, N.S., Bennett, C.J. (1994) *The Use of CFD as an Aid to Catalytic Converter Design*, ATA Proc. 4th International Conference Vol. 1 387-393

[33] Matthias Hettel, Daymo E., Schmidt T., Deutschmann O. (2019) *CFD-Modeling of Fluid Domains with Embedded Monoliths with Emphasis on Automotive Converters*, Chemical Eng. Process. -Process Intensification, 148(8) DOI: 10.1016/j.cep.2019.107728

[34] Weltens, H., Bressler, H., Terres, F., Neumaier, H., Rammoser, D. (1993*) Optimization of Catalytic Converter Gas Flow Distribution by CFD Prediction*, SAE Paper 930780 DOI: https://doi.org/10.4271/930780

[35] A. Romagnoli, A. Manivannan, S. Rajoo, M.S. Chiong, A. Feneley, A. Pesiridis, R.F. Martinez-Botas (2017*) A review of heat transfer in turbochargers,* Renewable and Sustainable Energy Reviews 79:1442-1460, DOI: 10.1016/j.rser.2017.04.119

[36] A. Trska (2012) *CFD Simulation of Exhaust Gases Flow through the Wastegate of Petrol Engines Turbocharger*, Master's Thesis, Brno University of Technology

[37] S. F. Benjamin and C. A. Roberts (2014) *Methodology for Modelling a Combined DPF and SCR Catalyst with the Porous Medium Approach in CFD* SAE International Journal of Engines, 7(4), 1997–2011. http://www.jstor.org/stable/26277905

[38] Q. Robert, J. Yin (2021) *Compressor Design, Operation and Performance*, Garrett Advancing Motion, Internal Trainings

[39] Xiao He, Xinqian Zhen (2018) *Flow instability evolution in high pressure ratio centrifugal compressor with vaned diffuser,* Experimental Thermal and Fluid Science Vol. 98, 719–73, ISSN 0894-1777

[40] Garrett Motion Inc (2020) Turbo Tech 102 - Advanced: Air Flow, https://www.garrettmotion.com/wp-content/uploads/2019/10/GAM_Turbo-Systems-102_Advanced.pdf

[41] K SERIES PARTS, https://www.kseriesparts.com/GAR-827690-0004.html

[42] JNA Performance, https://jnaperformance.com/products/atp-turbo-bolt-on-gt3076r-external-wastegate-turbo-subaru-2002-2007-wrx-2004-2019-sti-atp-sub-006

[43] Garrett Motion Inc. (2023) *2022 Sustainability Report,* https://www.garrettmotion.com/wp-content/uploads/2023/08/Garrett-2022-Sustainability-Report.pdf

[44] T.Anand, S.Jensen,P. Muthyala,R. Asvathanarayanan,R. Murugesan,A. Kumarasamy (2017). *Simulation of a Diesel Engine with Variable Geometry Turbocharger and Parametric Study of Variable Vane Position on Engine Performance*, Defence Science Journal 67(4), pg. 375, DOI: 10.14429/dsj.67.11451

[45] N. Watson, M.S. Janota (1982) *Turbocharging the Internal Combustion Engine*. 1st ed. London: The Macmillan Press Ltd., ISBN 0333242904.

[46] Chen, Q., J. Ni, X. Shi, Q. Wang, Q. Chen and S. Liu (2016*). Research on effect of wastegate diameter on turbocharged gasoline engine performance*. SAE Technical Paper, DOI: https://doi.org/10.4271/2016-01-1028

[47] Capiluppi, C. (2012). *Three Dimensional CFD Simulation of a Turbocharger Turbine for Motorsport Applications*, 1st ed. M. Sc Thesis, University PARMA, Italy

[48] Benajes J., J. Galindo, P. Fajardo and R. Navarro (2014*). Development of a segregated compressible flow solver for turbomachinery simulations.* Journal of Applied Fluid Mechanics 7(4), 673-682.